Photocatalytic H_2(g) Production from Polylactic Acid Containing Real Plastic Wastes Using Cu_7S_4/CdS Nanocomposites

RUKİYE ÖZTEKİN, DELİA TERESA SPONZA*
Department of Environmental Engineering
Dokuz Eylül University
Tınaztepe Campus, 35160 Buca/Izmir,
TURKEY

**Corresponding Author*

Abstract: - In this study, H_2(g) production from a real plastic wastes containing polylactic acid (PLA) using Cu_7S_4/CdS nanocomposites (NCs) was performed with photocatalytic degradation process. The effects of increasing pH values (3.0, 4.0, 5.0, 7.0, 9.0 and 11.0), photodegradation times (30, 60, 120, 180, 240 and 300 min), PLA concentrations (5, 10, 15 and 20 mg/l) and increasing using Cu_7S_4/CdS NCs concentrations (5, 10, 25, 50 and 100 mg/l) on H_2(g) production from a real plastic wastes containing PLA was investigated using Cu_7S_4/CdS NCs during photocatalytic degradation process. XRD, FESEM, EDX, TEM and XPS analyses were performed for characterization of Cu_7S_4/CdS NCs. PLA measurements were performed using an inductively coupled plasma mass spectrometry (ICP-MS). H_2(g) measurements were made in gas chromatography–mass spectrometry (GC-MS). Maximum 99.69% H_2(g) production efficiency was obtained after 240 min photocatalytic degradation time from 10 mg/l PLA in real plastic wastes, at pH=7.0, at 300 W UV-vis light and at 25^{o}C, using 50 mg/l Cu_7S_4/CdS NC dose, respectively. The operating data were defined with an Artificial Neural Network (ANN) model based on H_2 production. The experimental results were compared with the ANN model data and it was found that the model and laboratory data agree which other. The design of the photoreactor and the operational conditions for treat the PLA can be defined by ANN model. The reusability of Cu7S4/CdS NCs was applied during 40 cycles. The PLA photocatalytic capacity remained stable for 30 cycles as 99%, while the PLA uptake and photodegradation yields of PLA decreased slightly to 98% after 35 cycles. As a result, 98% regeneration was achieved for 50 mg/l Cu7S4/CdS NCs during 10 mg/l PLA degradation. The photocatalytic degradation process is a very effective, easy to apply, is economical and environmentally friendly for the removals of PLA from plastic and microplastic wastes from in environmental areas.

Key-Words: - Anilite/cadmium sulfide (Cu_7S_4/CdS) nanocomposite; Hydrogen gas [H_2(g)] production; Microplastics (MPs); Photocatalytic degradation process; Photoreforming; Polylactic acid [PLA, $(C_3H_4O_2)_n$].

Received: June 21, 2025. Revised: October 9, 2025. Accepted: December 8, 2025. Published: March 19, 2026.

1 Introduction

When plastic packaging is released to the receiving environment; 86% of it is collected in landfills or randomly dispersed into the environment, [1], [2], [3]. Plastic pollution is not just a global pollution problem; It also shows the unconscious waste of a very valuable resource that can be recycled and reused. The vast majority of polymers are synthesized from fossil fuels and especially petroleum derivatives, [1]. If all global plastic waste is recycled; It is estimated that approximately 3.5 billion barrels of oil can be saved every year, [1]. One of the most important problems in the spread of plastic recycling; Lack of awareness, suboptimal waste management, limited size of various chemicals, complexes and polymer products, [3].

Polymer fragments smaller than ≤ 5 mm are defined as microplastics (MPs) and are a group of plastics that are particularly problematic in terms of recycling, [4], [5], [6]. MPs formed by the decomposition of plastics over time; They are available in a wide variety of products, [5]. MPs are dispersed in very small sizes and very diluted; from oceans, [4], [5], [6], drinking water and salts, [7], [8], [9], almost everywhere in the world, making it very difficult to collect and reuse. The most important disadvantages of MPs are; Even recycling reusable plastics has its limitations. Because of this drawback, many polymers can only be processed into lower quality products. For example, only 7% of recycled poly(ethylene terephthalate) (PET) bottles can be remanufactured as plastic bottles, [3]. Waste management applied in plastic recycling; It is currently

far from sustainable and economical treatment of a wide range of plastic waste. More functional and useful new technologies are urgently needed to eliminate existing problems and transform polymers into valuable products after use.

Polylactic acid [PLA, $(C_3H_4O_2)_n$] is an environmental-friendly alternative to petroleum-derived plastic due to biodegradability and biocompatibility, [10], which can be used in the following sectors: packaging, agriculture, textiles, clinical sector, and others, [11]. In 2015, the global production of PLA was around 200 kt, [12], and it is expected to reach 560 kt in 2025, [13], with an increase of 180% over the past decade. Thus, its tremendous growth in single-use products has led to serious social problems, e.g., economical inefficiency, excess wastes, and associated environmental concerns, [14]. PLA is biodegradable, it takes decades to completely degrade in landfill, [15], and 60–100 days are also needed under elevated temperature (50 ± 5^{o}C) in composting conditions, [16]. These two routine degradation methods are not recommended choices since no material is recovered. In this regard, the chemical end-of-life scenario of short-life PLA is essential to determine its sustainability and circular economy, where monomer regeneration occurs, or value-added chemicals are produced. Chemical degradation of PLA generally includes hydrolysis, pyrolysis, alcoholysis, and ammonolysis, [17]. A serious of products were derived from the above recycling options, such as lactic acid, [18], [19], lactide, [20], [21], lactate ester, [22], [23], biofuel, [24], [25], and others, [26]. Hydrolysis occurs through random scission of the ester bond around 200^{o}C and the monomer of lactic acid is formed, which can further convert into new PLA and a variety of chemicals, [18]. Pyrolysis takes place via intramolecular transesterification of PLA and results in lactide over the range of 200–500^{o}C, [20], [21]. Alcoholysis allows the formation of lactate esters, known as green solvents, and they can be transformed into lactide, resulting in circular economy, [22], [23]. Ammonolysis depolymerizes PLA into alanine, which also expands the application of PLA wastes, [26].

In order to solve environmental problems and the global energy crisis; There is an urgent need for new, sustainable, safe and efficient green energy technologies. Hydrogen (H_2) energy generation with H_2 fuel cell; It is an emission-free energy conversion system and is a promising alternative energy source, [27], [28], [29], [30], [31]. In H_2 production; photocatalytic strategy, ambient temperature and ambient pressure parameters; It enables the collection of inexhaustible sunlight to produce chemical fuel, [32], [33], [34], [35], [36]. An ideal photocatalyst should utilize low-cost, broad-spectrum light, efficiently separate and transfer electrons and holes, and maintain sufficient band-edge potential. Since transition metal chalcogenides have a suitable band gap for a better solar spectrum response; It has been extensively investigated for H_2 production, [32], [37], [38], [39], [40]. Transition metal chalcogenide-based heterostructures such as CdS@CdTe@PDDA@Au_x, CdS@$(Cu_L$-B/M$)_4$ and CdSe QD/2Ni-MN for improved photocatalytic H_2(g) production; They can be used as versatile photocatalysts, [41], [42], [43]. Generally, these representative heterostructures are; They combine three functional parts: light absorbers, charge transfer channels, and redox active sites.

A new technology that has been recently implemented in the recycling of plastics, especially MPs; It is a photoreformation method in which H_2(g) is produced from an organic substrate and water using sunlight and a photocatalyst. The basic principle in the photoreformation method; It occurs by oxidizing the substrate to other organic molecules by the excited photocatalyst acting as an electron donor. Photogenerated electrons are in the next stage; They are transferred from the photocatalyst to the co-catalyst, reducing water to H_2(g). H_2(g) is a very valuable raw material that is frequently used in renewable energy applications as well as in the chemical, pharmaceutical and agricultural industries, [44]. Among the existing H_2(g) production technologies; Unlike steam reforming of fossil fuels, [45], or thermal-based approaches to convert plastic to oil, [46], the photoreformation method has many advantages. The most important advantages of photoreformation are: they can be operated at ambient temperature and pressure, they can use sunlight as the only energy input, and they can produce H_2(g) class fuel cells, [47]. Photocatalytic degradation of plastics, typically to MPs and CO_2(g), has been investigated for many years, [48], [49], [50]. With the photoreformation method, not only plastic waste is reduced; At the same time, a very important advantage is provided by producing very valuable chemical products industrially. The thermodynamics of the photoreformation process is almost energy neutral, [51]. In the photoreformation process, photoreformation of ethylene glycol at 25^{o}C requires $\Delta G° = 9.2$ kJ mol^{-1} and $E°cell = - 0.01$ V.

Cadmium sulfide (CdS) is inexpensive and widely used, its band gap is ≈ 2.4 eV; It is a photocatalyst that absorbs visible light, [52], [53], [54], [55]. The conduction band of CdS provides sufficient potential for the reduction of aqueous protons: holes in the valence band; It is sufficient in the oxidation of various hole cleaners for biomass and plastic waste, [56], [57], [58]. Hot carriers also cause major problems causing unwanted photo-corrosion of transition metal chalcogenides, [29], [30], [54], [55], [59]. In general, the performance of the bare CdS photocatalyst is poor without hybridization. Copper sulfides (Cu_2S), as a

popular cocatalyst, in reactions to form heterojunctions; They can combine with CdS, effectively reduce charge carrier recombination, and expand the optical response range, [60]. They exhibit a gradual alignment between Cu_2S and CdS after the formation of the p-n junction. It is generally accepted that under this term of band structure, hot electrons flow to the lower conduction band (CB) and the hole is transferred to the higher valence band (VB) under light excitation, [61]. The corresponding reduction in electron reducibility and hole oxidizability resulting from the above transfer mechanism; will limit their ability for wider reactions such as the production of H_2(g) from plastic reforming where strong oxidizability of the holes is required. This is with electrons remaining in the CB of the Cu_2S and holes on the CdS forming the Z-scheme photocatalyst; requires a better performance, [33], [62], [63]. However, the migration path of hot carriers at the Cu_2S/CdS heterojunction is rarely seen following the Z-scheme mechanism, [58], [64], [65]. Although, the photoreformation of simple molecules and biomass has been investigated in detail, [51], [66], [67], plastic substrates have been largely ignored. Making polymer recycling difficult; Complex structures, low water solubility and poor biodegradation also make the photoreformation method more difficult. There are only a few previous studies on the photoreformation of plastics: in one of them; While using expensive and ultraviolet (UV) absorbing TiO_2/Pt photocatalyst, [68], in another; toxic CdS/CdO_x quantum dots are used, [57].

Anilite/cadmium sulfide (Cu_7S_4/CdS) heterostructures with high quality interface are formed by solution-mediated ion exchange method. The ion exchange method has become a versatile synthesis strategy for generating ionic heterostructures using an existing crystal lattice as a temple; thus, it can regulate the composition and performance of materials by changing the central ion without changing the particle size and morphology, [69], [70], [71], [72], [73]. The soft Lewis acid cations Cu^+ in the Cu_7S_4 nanoparticle, driven by the dissolution energies and Lewis acid base interactions, can be gradually replaced by the harder Cd^{+2}. By controlling the changeover time; Nanoparticles with various Cu_7S_4/CdS ratios can be easily obtained, [38], [39]. Hybrids can effectively support H_2(g) production; The Z-order electron transfer mechanism is illustrated by the strong and long-lasting holes in the CdS domain. Based on precise ratio tuning and well-defined structure, there is a correlation between the Cu_7S_4/CdS ratio and the stability of photocatalysts. In showing that the Cu_7S_4/CdS ratio is critical in the electron accumulation in the Cu_7S_4 area; Single nanoparticle impact studies are a potential scope complement for bulk catalyst research. By maintaining hot holes and hot electrons in these heterostructures; The activity of H_2(g) production from PLA plastic reforming is increased.

In this study, H_2(g) production from a real plastic wastes containing PLA using Cu_7S_4/CdS NCs was investigated with photocatalytic degradation process. Effects of different pH values (3.0, 4.0, 5.0, 7.0, 9.0 and 11.0), increasing photodegradation times (30, 60, 120, 180, 240 and 300 min), increasing PLA concentrations (5, 10, 15 and 20 mg/l) and increasing Cu_7S_4/CdS NCs concentrations (5, 10, 25, 50 and 100 mg/l) on H_2(g) production from real plastic wastes containing PLA was investigated during photocatalytic degradation process. XRD, FESEM, EDX, TEM and XPS analyzes were performed for characterization of Cu_7S_4/CdS NCs generated under laboratory conditions. A mathematical model namely ANN was generated to compare the experimental data during H_2 production.

2 Materials and Methods

2.1 Experimental Materials

Cadmium (II) chloride hemi(pentahydrate) ($CdCl_2.5/2H_2O$, 98%), Di-tert-butyl disfulide (DTBDS, ≥ 98%) and Copper (II) chloride dehydrate ($CuCl_2.H_2O$, 99.99%) were purchased from Sigma-Aldrich (Germany). Polylactic acid (PLA), Oleylamine (OA, 98%), Tri-n-octylphosphine (TOP, 98%) and 1-Octadecene (ODE, ≥ 98%) were purchased from Sigma (Germany). Dibenzyl ether ($C_4H_{14}O$, 95%), sodium sulfide nonahydrate ($Na_2S.9H_2O$, 99.99%), sodium sulfite anhydrous (Na_2SO_3, ≥ 98%), acetone (CH_3COCH_3, 99.99%) and Ethanol (C_2H_5OH, 99.99%) were purchased from Aldrich (Germany).

2.2 Preparation of Cu_7S_4 Nanocomposites

Cu_7S_4 NCs were produced using a hot injection method described in the literature, [74]. First, 341 mg of $CuCl_2.2H_2O$, 48 ml of Oleylamine and 12 ml of 1-Octadecene were sequentially placed in a 100 ml three-neck round-bottom flask equipped with a reflex concentrator. After sparging Argon gas [Ar(g)] from this three-necked round-bottom flask and vacuuming three times; placed under an Ar(g) stream, held at 100°C for 30 min; then kept at 200°C for 60 min. The solution was cooled to 180°C and then 8 ml of di-tert-butyl disulfide was rapidly injected under Ar(g); the solution quickly turned from yellow to brown. After continuing for 45 min, the brown color became clearer. The suspension was cooled to 25°C room temperature in an ice water bath. The product was added to the reaction mixture in the ratio of ethanol/acetone: 1/1; It was isolated by centrifugation at 5000 rpm for 5 min. To be used in product, characterization and subsequent reactions; washed three times with acetone and dried under vacuum at 70°C.

2.3 Application of Cation Exchange Reactions with Cd^{+2}

Partial cation exchange reactions with Cd^{+2} were performed according to a procedure in the literature, [74]. 210 mg of $CdCl_2.5/2H_2O$, 8 ml of Oleylamine, 2 ml of 1-Octadecene and 15 ml of benzyl ether were added sequentially to a 100 ml three-neck round-bottom flask. Ar(g) was sparged from the three-neck round bottom flask and placed under a stream of Ar(g); vacuumed three times, and held at 100°C for 30 min. During this time, 100 mg of Cu_2S nanoparticles (NPs) were re-suspended in 5 ml of Tri-n-octylphosphine and sonicated for 60 min. The temperature was then cooled to 50°C and the nanoparticle/ Tri-n-octylphosphine suspension was rapidly injected into the reaction flask, allowing it to react for the specified time. After the desired reaction time, the reaction was terminated by injecting 8 ml of ice-cold acetone into the bottle. The product was precipitated by the addition of ethanol, and recovered by centrifugation at 8000 rpm for 5 min. The product is to remove superficial Oleylamine; It was washed several times with the hexane/acetone: 1/1 mixture, then dried under vacuum at 70°C for use in characterization and subsequent reactions.

2.4 Pretreatment of Substrate

50 mg/l polymer was mixed at 300 rpm with our adaptation from the procedure described in the literature, [75]. Then put in a closed bottle; It was immersed in 2 M aqueous semiconductor grade KOH at 40°C for 24 h.

2.5 Generation of Photocatalytic H_2(g)

Evaluation of the photocatalytic activity of the prepared composite; It was carried out at 25°C ambient temperature. Na_2SO_3 and Na_2S were used as hole scavengers in the photocatalytic H_2(g) evolution. 2 mg of catalyst was dissolved by sonication in an aqueous solution of 0.25 M Na_2SO_3 and 0.35 M Na_2S in a 50 ml glass vial. After removal of O_2(g) by sparging N_2(g), the photocatalysis process was carried out at room temperature at 25°C; here a 300 W xenon lamp for UV-vis light irradiation equipped with a 420 nm cut-off filter is used as a light source to accelerate the photocatalytic reaction by triggering it. The H_2(g) concentration was measured using gas chromatography–mass spectrometry (GC-MS). For PLA degradation: 10 ml sample is taken from 10 M NaOH solution containing powdered 100 mg/ml PLA concentration; placed in a glass bottle and 2 mg of catalyst was added to it. Before irradiation, the bottle containing the catalyst and the aqueous solution of PLA, to ensure that an adsorption/desorption equilibrium is established between the catalyst and PLA molecules; It was stirred at 25°C at room temperature in the dark for 30 min. Finally, the reaction solution exposed to visible light for 4 h was able to measure the concentration change of Polylactic acid with 1H-NMR and 13C-NMR; separated from the catalyst by centrifugation. The average intensity of the irradiation was determined by a photo radiometer (PL-MW2000, Perfect Light). The following equation was used to calculate the quantum efficiency.

2.6 Mechanism of Stoichiometric H_2(g) Conversion

A volume of 4 ml was taken from 1 M KOH; Samples containing 10 mg of substrate were prepared and irradiated for photocatalysis. H_2(g) conversion (%) was calculated as in Eq. (1), [76], [77]:

$$H_2 \text{ conversion } (\%) = 100 \text{ x } \frac{n_{H_2,exp} n^{-1}_{substrate,exp}}{n_{H_2,ideal} n^{-1}_{substrate,ideal}} \quad (1)$$

where; n_{H2},exp: is the H_2(g) measured in experiment (mol), $n_{substrate,exp}$: is the substrate used in experiment (mol), and $n_{H2,ideal} n_{substrate,ideal}^{-1}$: is the ideal ratio of moles H_2(g) to substrate, respectively.

2.7 Power Calculation

Power output from generated H_2(g); It was calculated according to Eq. (2):

$$\text{Power (W)} = \frac{V_{H_2} n_{H_2} \rho_{H_2} u_{H_2}}{t_{irr}} \quad (2)$$

where; V_{H2} : is the molar volume of H_2(g) (24.47 l/mol at 25°C), n_{H2} : is the moles of H_2(g) produced, ρ_{H2} : is the density of H_2(g) (8.235×10^{-5} kg/l at 25°C), u_{H2} : is the lower heating value of H_2(g) (120×10^6 J/kg), and t_{irr} : is the irradiation time (s), respectively.

2.8 Calculation of Apparent Quantum Yield (AQY)

AQY was calculated using Eq. (3):

$$AQY\ [\%] = \frac{number\ of\ reacted\ electrons}{number\ of\ incident\ photons}\ x\ 100 \quad (3)$$

The number of incident photons was measured using a light spectroradiometer (S-2440 model II Hidamari mini, Soma Optics, Ltd., Tokyo, Japan), and the number of reacted electrons was calculated from the evolved hydrogen. The H_2 evolution rate was measured in the same reaction system as other photocatalytic reactions. To determine the wavelength dependence of AQY, Pt (0.5 wt%)-deposited Cu_7S_4/CdS photocatalyst was irradiated with monochromatic light generated using a Xe lamp, and the light was sent through band-pass filters with central wavelengths of 380, 420, 460, 500, 540, or 580 nm (Asahi Spectra Co., Tokyo, Japan).

2.9 Evaluation of the Reusability of Prepared Photocatalyst

Reusability tests were conducted in test tubes (32 ml) sealed with a rubber cap under an Argon gas [Ar(g)] atmosphere. The prepared Pt (0.5 wt%)-deposited Cu_7S_4/CdS NCs (50 mg) and 70ºC of 10 M NaOH solution (5 ml) were prepared in the reaction cell. Initially, 10 mg of substrate was added to the solution, and after 50 h (α-cellulose and albumin) or 20 h (polyethylene), the substrate was added again. A Xe lamp was used as the light source. A 0.2 ml aliquot of the evolved gas was collected using a gastight syringe, and the sampled gas was injected into the gas chromatograph (GC) to determine the amount of evolved H_2. Degassing was performed every 10 h.

2.10 Characterization

2.10.1 X-Ray Diffraction (XRD) Analysis

Powder XRD patterns were measured on a Shimadzu XRD-7000, Japan diffractometer using Cu Kα radiation (λ = 1.5418 Å, 40 kV, 40 mA) at a scanning speed of 1º /min in the 10-80º 2θ range.

2.10.2 Field Emission Scanning Electron Microscopy (FESEM) Analysis

The morphological features and structure of the experimental samples were determined by Field Emission Scanning Electron Microscopy (FESEM) (FESEM, Hitachi S-4700).

2.10.3 Energy Dispersive X-Ray (EDX) Spectroscopy Analysis

The elements on the surface of the experimental samples were analysed using energy dispersive X-ray analysis (EDX) with EDX spectrometry device (TESCAN Co., Model III MIRA).

2.10.4 Transmission Electron Microscopy (TEM) Analysis

The obtained experimental samples were collected and harvested by centrifugation (8000 rpm, 5 min), washed twice with deionized H_2O, and resuspended in ethanol (C_2H_6O) and dripped onto a carbon-coated copper (Cu) Transmission Electron Microscopy (TEM) grid. Vacuum drying then occurred to the experimental samples for 24 h at 25ºC. The dry samples on the Cu grid were viewed and examined by TEM Analysis recorded in a JEOL JEM 2100F, Japan under 200 kV accelerating voltage. The size and structure of the experimental samples were identified with TEM analysis.

2.10.5 X-Ray Photoelectron Spectroscopy (XPS) Analysis

The valence state of the experimental samples were investigated and was analyzed using XPS (ESCALAB 250Xi, England). XPS used an Al Kα source and surface chemical composition and reduction state analyses was done, with the core levels recorded using a pass energy of 30 eV (resolution approximately 0.10 eV). The peak fitting of the individual core-levels was done using XPS-peak 41 software, achieving better fitting and component identification. All binding energies were calibrated to the C 1s peak originating from C–H or C–C groups at 284.6 eV.

2.10.6 Inductively Coupled Plasma Optical Emission Spectrometry (ICP-OES) Analysis

ICP-OES analysis was employed to determine the H2 gas, In and Ga contents and measured on a Varian 720-ES (Varian Inc., Palo Alto, CA, USA). Solutions from the powder were prepared via acidic leaching. Respective metals were detached from silica in a sealed container using saturated hydrochloric acid (35%) at 120ºC. The spectroscope was three-point calibrated with a commercially available, diluted standard for In and Ga. Mass fractions of carbon (C), hydrogen (H_2), nitrogen (N_2), and sulfur (S_8) were determined by combustion analysis (CHN), executed on a EuroEA Elemental Analyzer (HEKAtech GmbH, Wegberg, Germany).

2.10.7 Diffuse Reflectance UV-vis Spectra (DRS) Analysis

UV-vis Diffuse reflectance spectroscopy (UV-vis DRS) of specimens was examined using a SHI-MADZU spectrometer model UV-1240 (ranging from 200–900 nm with $BaSO_4$ as reference).

2.10.8 Inductively Coupled Plasma Mass Spectrometry (ICP-MS) Analysis

The Agilent 8800 ICP-MS instrument (Agilent Technologies, Japan) was used to determine different concentrations of polyethylene terephthalate and polylactic acid. For analysis, the samples were acid digested in closed Savillex® PFA beakers prior to ICP-MS. 5 ml of suspended sample in PBS was centrifuged at 10000 ×g for 30 min, after which the supernatant was removed. The resulting pellet was acid digested with 1.5 ml of 14 mol/l HNO_3 and 0.5 ml of 9.8 mol/l H_2O_2. The closed beakers were heated to 115°C overnight on a hot plate. After complete mineralization, the digestates were evaporated at 90°C until dryness, then redissolved in 2.0 ml of 0.35 mol/l HNO_3. This solution was further diluted with 0.35 mol/l HNO_3 and rhodium (Rh) was added as the internal standard (final concentration = 2 µg/l) to compensate for potential matrix effects and/or signal instability.

2.10.9 Gas Chromatography–Mass Spectrometry (GC-MS) Analysis

Gas chromatography–mass spectrometry (GC-MS) and gas chromatograph (GC) (Agilent Technology model 6890N) equipped with a mass selective detector (Agilent 5973 inert MSD). Mass spectra were recorded using a VGTS 250 spectrometer equipped with a capillary SE 52 column (HP5-MS 30 m, 0.25 mm ID, 0.25 μm) at 220°C with an isothermal program for 10 min. The initial oven temperature was kept at 50ºC for 1 min, then raised to 220ºC at 25ºC/min and from 200 to 300ºC at 8ºC/min, and was then maintained for 5.5 min. High purity He(g) was used as the carrier gas at constant flow mode (1.5 ml/min, 45 cm/s linear velocity). All H_2(g) measurements of the experimental samples were made in the GC-MS device.

2.11 Electrochemical Measurements

The single-nanoparticle impact electrochemistry experiments were carried out using an Axopatch 200B integrating patch-clamp amplifier (Molecular Devices) inter faced to a PC through a Digidata 1550B digitizer (Molecular Devices). The Axopatch was used in V-clamp mode with whole cell β=1andthe low-pass filter set to10kHz. Current response was recorded using pClamp 10.4 Axoscope software (Molecular Devices) with a 100 kHz sampling rate. Current spikes and charge accumulation were analysed and integrated using pClamp 10.4 Clampfit software (Molecular Devices), and histograms of the events with corresponding Gaussian fits were created using Origin software. All experiments were performed using a two-electrode setup placed in a lab-built Faraday cage. A carbon microelectrode was used as the working electrode in all experiments, and the diameter was calculatedas16 μm. This electrode was fabricated by forming a C layer on a 30 nm diameter quartz capillary (Sutter Instrument Co.) and making connection to the C with Cu wire and sealed with Epoxy. The C electrodes were exposed via mechanical polishing and rinsed thoroughly before experiment. An Ag/AgCl wire was used as the counter and quasi-reference electrode (QRE) in all single-nanoparticle collision experiments. All potentials are reported as V vs Ag/AgCl QRE.

2.12 Statistical Analysis

ANOVA analysis of variance between experimental data was performed to detect F and *P* values. The ANOVA test was used to test the differences between dependent and independent groups, [78]. Comparison between the actual variation of the experimental data averages and standard deviation is expressed in terms of F ratio. F is equal (found variation of the date averages/expected variation of the date averages). *P* reports the significance level, and d.f indicates the number of degrees of freedom. Regression analysis was applied to the experimental data in order to determine the regression coefficient R^2, [79]. The aforementioned test was performed using Microsoft Excel Program.

All experiments were carried out three times and the results are given as the means of triplicate samplings. The data relevant to the individual pollutant parameters are given as the mean with standard deviation (SD) values.

3 Results and Discussions

3.1 Characterizations

3.1.1 XRD Analysis

The results of XRD analysis was obtained after H_2(g) production from real wastes of PLA using Cu_7S_4/CdS nanocatalyst with photoreforming process (Fig. 1). The characterization peaks were found at 2θ values of 25.64º, 27.11º, 28.36º, 37.45º, 44.25º, 47.58º, 51.12º, 53.24º, 56.71º and 68.87º, respectively, and which can also be indexed as (101), (210), (204), (312), (100), (210), (112), (301), (203) and (212), respectively (Fig. 1).

* Figure 1 can be found in the Appendix section.

XRD pattern was applied to confirm the crystal structure of Cu_7S_4 and Cu_7S_4/CdS compositions with different exchange time (Fig. 1). The diffraction peaks of the Cu_7S_4 nanoparticle can be well indexed to the orthorhombic Cu_7S_4 (PDF#33-0489). After 20 min of reaction, the peaks of CdS (PDF#41-104) emerged and held as the main portion of XRD pattern after just 40 min reaction.

3.1.2 FESEM Analysis

The morphological features of Cu_7S_4/CdS nanocatalyst was characterized through FESEM images before photoreforming process (Fig. 2a) and after photoreforming process (Fig. 2b), respectively, for H_2(g) production from real wastes of PLA.

* Figure 2 can be found in the Appendix section.

3.1.3 EDX Analysis

The results of EDX analysis was measured after H_2(g) production from real wastes of PLA using Cu_7S_4/CdS nanocatalyst with photoreforming process (Fig. 3).

* Figure 3 can be found in the Appendix section.

The TEM-EDS mapping further confirms the heterogeneous distribution of Cd and Cu, and Cd content has been defined as 0.46 (Cu_7S_4/CdS-0.46), 0.88 (Cu_7S_4/CdS-0.88) and 0.95 (Cu_7S_4/CdS-0.95) by

weight percentage, with growing exchange time of 20 min, 60 min and 90 min, respectively.

3.1.4 TEM Analysis

The TEM images of Cu_7S_4/CdS nanocatalyst was observed during H_2(g) production from real wastes containing PLA after photoreforming process (Fig. 4).

* Figure 4 can be found in the Appendix section.

The Cu_7S_4/CdS heterojunctions were obtained through a solution-mediated cation exchange process between Cu_7S_4 and Cd^{2+}. Driven by solvation energies and Lewis acid-base interactions, the soft Lewis acid cations Cu^+ in the Cu_7S_4 NPs can be replaced by harder Cd^{2+} gradually. Morphology of the as-fabricated Cu_7S_4 and exchanged products were checked by TEM, which showed the spherical structures of crystalline Cu_7S_4 with an average diameter of about 30 nm (Fig. 4). Cd^{2+} exchange did not obviously affect the initial morphology of Cu_7S_4 (Fig. 4), but a distinct interface can be observed. The Cd^{2+} propagated solely along one side of Cu_7S_4 via heterogeneous nucleation during the exchange process (Fig. 4), which is attributed to the lower energy barrier of this process in comparison to homogeneous nucleation on Cu_7S_4 , [80] As TEM image shown in Fig. 4, lattice fringes of 0.198 nm and 0.208 nm can be assigned to the (110) plane of hexagonal CdS and (400) plane of orthorhombic Cu_7S_4, respectively, confirming the formation of Cu_7S_4 /CdS NCs.

3.1.5 XPS Analysis

The XPS analysis of Cu_7S_4/CdS nanocatalyst was obtained to H_2(g) production from real wastes of PLA after photoreforming process (Fig. 5).

* Figure 5 can be found in the Appendix section.

XPS analysis was carried out to analysed the chemical composition of the prepared samples and identify the chemical status of Cu, S and Cd element in the samples. The binding energies recorded at 932.40 and 952.30 eV assigned to Cu^+, 161.40 and 162.50 eV assigned to S_2, which are consistent with Cu_7S_4 (Fig. 5). The peaks of Cu^+ slightly left-shift with increasing exchange time. In contrast, the peaks at 404.80 eV (Cd $3d^{5/2}$) and 411.60 eV (Cd $3d^{3/2}$) of Cd XPS spectrum slightly right-shifted (Fig. 5), indicating that the heterojunction between Cu_7S_4 and CdS was setup.

3.1.6 ICP-OES Analysis

This was demonstrated by ICP-OES experiments (Fig. 6). Because of the dominate portion of Cd relative to Cu after 120 min exchanging (almost 100%, Fig. 6), we applied it as the pristine CdS to keep in morphology consistent with other samples

* Figure 6 can be found in the Appendix section.

3.1.7 DRS Analysis

DRS analysis resuls were determined at Fig. 7. Comparison of UV-vis-NIR DRS spectra of the prepared CdS/Cu7S4x (x=0, 0.09, 0.18, 0.33, 0.45, 0.57) were illustrated at Fig. 7.

* Figure 7 can be found in the Appendix section.

To evaluate the quantitative activity and wavelength dependence of the photocatalytic reaction, the action spectra of each photocatalyst were measured. Focusing on the action spectrum of pure CdS, the quantum yields also decreased from approximately 500 nm, where the absorption spectrum attenuated and reached almost 0% at 580 nm. On the other hand, pure Cu_7S_4 absorbs the entire visible light range, but the photocatalytic reaction proceeds in the ultraviolet region. As the baseline of the DRS of CdS decreased (Fig. 7), it can be seen that there are many defect levels. Since the absorption derived from the defect level is not used in the photocatalytic reaction and is considered to be radiated as heat, the quantum yield was very low in the wavelength region after 480 nm. The quantum yield of the Cu_7S_4/CdS NCs was higher than that of a single photocatalyst in most wavelength regions. In particular, the apparent quantum yield at 480 nm significantly improved, reaching approximately 20%. Furthermore, in the visible light region, we achieved a quantum yield of 2.0%. Charge carrier transfer between Cu_7S_4 and CdS is one of the reasons why the apparent quantum yield was higher than that of a single photocatalyst or conventional reports (Fig. 7). N_2 adsorption-desorption isotherms of CdS and Cu_7S_4 /CdS NCs-0.33 heterostructure (Fig. 8).

* Figure 8 can be found in the Appendix section.

3.2 Effect of Increasing pH Values

Increasing pH values (3.0, 4.0, 5.0, 7.0, 9.0 and 11.0) was examined for H_2(g) production with photocatayltic degradation process from real plastic wastes containing PLA, at 300 W UV-vis light and at 25°C (Fig. 9). 58.31%, 84.52%, 92.65%, 81.08% and 72.34% H_2(g) production efficiencies were measured at pH=3.0, pH=4.0, pH=5.0, pH=9.0 and pH=11.0, respectively, after Photocatayltic degradation process from of PLA in real plastic wastes, at 300 W UV-vis light and at 25°C (Fig. 9). The maximum 99.27% H_2(g) production efficiency was obtained after photocatayltic degradation process from PLA in real plastic wastes, at pH=7.0, at 300 W UV-vis light and at 25°C, respectively (Fig. 9).

* Figure 9 can be found in the Appendix section.

The pH of the solution plays a critical role in the photocatalytic process. In this research, the variation in pH was studied using 10 mg/l CdS. When the rate of photodegradation increases, it leads to an increase in solution pH value. This enhancement is probably due to the greater generation of hydroxyl radicals ($OH^{\bullet}$) at neutral pH levels, [36]. In Fig. 9, at pH = 7.0, the main absorbance peak is reduced the most, indicating the highest level of PLA degradation under light. The lowest degradation of PLA was observed at pH=3.0, possibly due to the abundance of H^+ ions in acidic media, which likely promotes the detachment of PLA from the catalyst surface and reduces the degradation rate, [37]. The results show that the optimized pH is 7.0.

3.3 Effect of Increasing Photocatalytic Degradation Time

Increasing photocatalytic degradation times (30, 60, 120, 180, 240 and 300 min) were operated for H_2(g) production with photocatalytic degradation process from PLA real plastic wastes, at 300 W UV-vis light, at pH=7.0 and at 25ºC, respectively (Fig. 10). 46.24%, 62.39%, 71.22%, 80.27%, 87.73% H_2(g) production yields were obtained after 30 min, 60 min, 120 min, 180 min and 300 min, respectively, after photocatalytic degradation process from PLA real plastic wastes, at 300 W UV-vis light, at pH=7.0 and at 25ºC, respectively (Fig. 10). The maximum 99.69% H_2(g) production efficiency was observed after 240 min with photocatalytic degradation process from PLA real plastic wastes, at 300 W UV-vis light, at pH=7.0 and at 25ºC, respectively (Fig. 10).

* Figure 10 can be found in the Appendix section.

3.4 Effect of Increasing PLA Concentrations

Increasing PLA concentrations (5, 10, 15 and 20 mg/l) were examined for H_2(g) production with photocatayltic degradation process from PLA real plastic wastes, after 240 min, at 300 W UV-vis light, at pH=7.0 and 25ºC, respectively (Fig. 11). 68.07%, 81.76% and 57.65% H_2(g) production yields were measured after 5 mg/l, 15 mg/l and 20 mg/l PLA, respectively, after photocatayltic degradation process from PLA real plastic wastes after 240 min, at 300 W UV-vis light, at pH=7.0 and at 25ºC, respectively (Fig. 11). The maximum 99.52% H_2(g) production efficiency was obtained at 10 mg/l PLA after photocatayltic degradation process from PLA plastic real wastes, after 240 min, at 300 W UV-vis light, at pH=7.0 and at 25ºC, respectively (Fig. 11).

* Figure 11 can be found in the Appendix section.

The degradation efficiency as a function of irradiation time is presented in Fig. 11. The efficiency increased with time, reaching 100% degradation after 240 min. As visible-light irradiation time increases on the semiconductor, electron-hole pairs are generated by the incident photons, initiating the photocatalytic process. The electron-hole pairs participate in reduction and oxidation reactions, respectively, leading to the cleavage of the aromatic ring of PLA; therefore, the PLA was mineralized.

3.5 Effect of Increasing Cu_7S_4/CdS NCs Concentrations

Different Cu_7S_4/CdS NCs concentrations (5, 10, 25, 50 and 100 mg/l) were operated for the efficient H_2(g) production with photocatayltic degradation process from PLA real plastic wastes, after 240 min, at 10 mg/l PLA, at 300 W UV-vis light, at pH=7.0 and at 25ºC, respectively (Fig. 12). 43.05%, 65.43%, 80.51% and 92.37% H_2(g) production efficiencies were found at 5 mg/l, 10 mg/l, 25 mg/l and 100 mg/l Cu_7S_4/CdS NCs, respectively, after photocatayltic degradation process from PLA real plastic wastes, after 240 min, at 10 mg/l PLA, at 300 W UV-vis light, at pH=7.0 and at 25ºC, respectively (Fig. 12). Maximum 99.64% H_2(g) production yield was obtained at 50 mg/l Cu_7S_4/CdS NCs, after photocatayltic degradation process from PLA real plastic wastes, after 240 min, at 10 mg/l PLA, at 300 W UV-vis light, at pH=7.0 and at 25ºC, respectively (Fig. 12).

* Figure 12 can be found in the Appendix section.

The results proved that catalyst could improve the photocatalytic processes. At low nanocomposite doses the PLA degradation efficiencies is low. Initially, as the photocatalyst concentration increased, the degradation efficiency increased. Increasing the amount of photocatalyst leads to a higher number of active sites on the photocatalyst surface and an increase in the generation of hydroxyl and superoxide radicals. However, beyond an optimal concentration, the efficiency decreases due to the suspension preventing light penetration and the aggregation of particles.

3.6 Photrocatalytic Degradation Mechanisms

The photocatalytic H_2-production activity of pristine CdS and Cu_7S_4, as well as Cu_7S_4/CdS NCs compositions under visible light irradiation ($\lambda > 420$ nm) are then performed with Na_2S and Na_2SO_3 as hole scavengers. The heterostructures shown splendid promotion compare with pristine Cu_7S_4 and CdS, revealing the boosted separation of photogenerated carriers in Cu_7S_4/CdS NCs compositions. It is noticed that Cu_7S_4/CdS-0.88 and Cu_7S_4/CdS-0.95 exhibit

sufficient stability. No significant activity loss was observed for the most active Cu_7S_4/CdS-0.88 heterostructure during 25 h of 5 cycles. In comparison, decreased H_2 production rate can be seen from the Cu_7S_4/CdS-0.46. We suppose that the CdS domain serves as a reservoir for hot holes, it was anticipated that the oxidation potentials of these holes would depend on the size of the CdS itself. It is proposed that small portion of CdS domain may cause the accumulation of photogenerated holes deeper in their VB to induce the oxidization of S^{2-}. In this case, to increase CdS-content can inhibit the photo-corrosion, which has been demonstrated by the excellent stability of Cu_7S_4/CdS-0.88 and Cu_7S_4/CdS-0.95.

By combining the bandgap energies and estimated the conduction band (CB) potentials of the Cu_7S_4 and CdS, the corresponding band structures are established in Fig. 13. The optical bandgaps and MottSchottky plots for Cu_7S_4 (Fig. 13a and 13b), CdS (Fig. 13c and 13d) were shown in Fig. 13.

* Figure 13 can be found in the Appendix section.

The photocatalysis on Cu_7S_4/CdS involves desirable direct Z-scheme charge transfer (Fig. 14a) and efficiency-reducing Type-II recombination processes (Fig. 14a). We carried out Electron paramagnetic resonance (EPR) and transient absorption (TA) measurement to confirm the presence of direct Z-scheme carrier immigration pathway in this Cu_7S_4/CdS heterojunction. We used 5,5-dimethyl-1-pyrroline N-oxide (DMPO) as a spin trap to identify radical species involved in the catalytic reaction.

* Figure 14 can be found in the Appendix section.

Fig. 14b shown the EPR spectra of Cu_7S_4, CdS, and Cu_7S_4/CdS-0.88. The reaction solution was measured both under dark environment and exposed to light irradiation for 10 min. Distinct signals were observed in spectrum for Cu_7S_4/CdS-0.88, identical but weak signals for CdS, and negligible signals for Cu_7S_4 under light condition. The signals are consistent with theoretical simulation of hydroxyl radical ($OH^{\bullet}$) radical species. Comparatively, not any noticeable signal was found under dark condition for all photocatalysts. The $OH^{\bullet}$ radical signals demonstrate that the holes localize in VB of CdS which possesses strong oxidization capacity. Meanwhile, the TA spectra of free CdS and Cu_7S_4/CdS-0.88 at indicated time delay safter 400 nm excitation is shown in Fig. 14c and 14d, respectively. The broad feature centered at ~ 630 nm in absorption spectrum can be attributed to trapped holes in CdS, [81], [82]. This absorption in CdS descended during 950ps after light excitation while in Cu_7S_4/CdS-0.88 heterojunction, the descent process delayed up to 6000 ps, evidencing the prolonged lifetime of holes in Cu_7S_4/CdS-0.88. Traditional on-off photocurrent responses of bare Cu_7S_4, CdS and Cu_7S_4/CdS-0.88 NCs have been investigated. In addition, the Electrochemical impedance spectroscopy (EIS) measurements were carried out in dark conditions. A clear decrease in the diameter of the Nyquist plot for Cu_7S_4/CdS-0.88 sample, suggesting a low resistance for interfacial charge transfer from catalysts to reaction molecules, which is consistent with transient photocurrent responses results. Besides traditional on-off photo current response, single nanoparticle impact electrochemistry was applied to analysed the properties of individual nanoparticles. The single-nano particle collision detection is a powerful analytical method to study electron-transfer kinetics at a true single-particle level. It has become potential scope complement for catalytical property investigation, considering its higher chemical resolution (pA range) compared to bulk test, [83], [84]. A 16 μm diameter carbon microelectrode was used as the working electrode in all experiments, as illustrated in Fig. 15a. Based on the diffusion and the electrophoresis of nanoparticles, they can collide with electrode and exchange electrons. A patch clamp amplifier was used to record the transient current with very high time evolution. The raw curves of current transients by collisions of Cu_7S_4/CdS-0.46 and Cu_7S_4/CdS-0.88 were determined.

* Figure 15 can be found in the Appendix section.

Fig. 15b shows a typical signal section extract, and collision behaviours are characterized by discrete events. The shape of the current spike and the duration of the transient are highly reproducible due to the high uniformity of the nano-structures. Positive voltage (0.6 V vs. Ag/AgCl) was supplied to obtain adequate collision frequency for statistical analysis. The current response distributions were integrated. All as-prepared Cu_7S_4/CdS NCs shown sharp positive spikes, which clearly demonstrates the electron transfer from nanoparticles to substrate electrode. Fig. 15c and 15d compared current response in dark, and typical current pulses can be observed. In Cu_7S_4/CdS heterojunction, electron redistribution occurs after the p-n junction forms. Electrons will transfer from CdS to Cu_7S_4 through the close interconnection to equilibrate their Fermi levels. Negative Cu_7S_4 domain should directly impact the electrode surface due to electrical attraction force and then electrons transfer happens. The amounts of transferred electrons from Cu_7S_4/CdS-0.88 in dark is slightly higher than that from Cu_7S_4/CdS-0.46. Since a larger portion of Cu_7S_4 exist in Cu_7S_4/CdS-0.46, there should be more electrons transferred to the Cu_7S_4 from CdS after the formation of p-n junction. However, Cu_7S_4/CdS-0.88 exhibits better capability for electrons

transfer to the electrode. We propose that the electrons in Cu_7S_4/CdS-0.88 are more negative than that in Cu_7S_4/CdS-0.46, possessing stronger ability for transferring electrons. Under light irradiation (> 420 nm), average event charge response of Cu_7S_4/CdS-0.88 (Fig. 15f) located at 756.3fC, significantly exceeds the amount of Cu_7S_4/CdS-0.46 (158.7fC, Fig. 15e), indicating more enriched photogenerated electrons in Cu_7S_4/CdS-0.88 and stronger electron transformation capability. This result is also in accordance with photocatalytic H_2 production performance. Considering the much smaller size of Cu_7S_4 in Cu_7S_4/CdS-0.88 than Cu_7S_4/CdS-0.46, the electrons should accumulate to even higher level in Cu_7S_4 domain of Cu_7S_4/CdS-0.88 under light irradiation, which favour the efficient electron transfer and reaction.

Since the electrons and holes in Cu_7S_4/CdS-0.88 maintain high reducibility and oxidizability, respectively. Plastic waste, which are widely used and causing an expanding disposal issue, were used as feedstock for visible light-driven H_2 generation without any other hole scavengers. Results showed significantly enhanced H_2 evolution and polylactic acid degradation performance for Cu_7S_4/CdS-0.88 compare with other Cu_7S_4/CdS heterostructures (Fig. 16a and 16b).

* Figure 16 can be found in the Appendix section.

Cu_7S_4 provided improved photocatalytic H_2 evolution performance to pristine CdS, serves as a more excellent cocatalyst than reported NiS or MoSX, [85], [86], [87]. Furthermore, the comparisons of photocatalytic H_2 production performance over the Cu_7S_4/CdS-0.88 and reported similar photocatalysts were observed. On oxidization half-reaction, we analysed the reaction mixtures and identified organic oxidation products by nuclear magnetic resonance (NMR). ^{13}C NMR (Fig. 16c) and ^{1}H NMR (Fig. 16d) suggest that Polylactic acid in NaOH hydrolyses to sodium lactate (peak a and b), and then oxidized to CO_3^{2-} (peak c) and small quantities of formate (peak d), acetate (peak e). The high pH solution can cause the formation of a very thin layer of oxide shell on the catalysts, which further enhances their stability. The H_2 production rate remained fairly constant during 30 h of six cycles, demonstrating the high stability of Cu_7S_4/CdS heterojunction system (Fig. 16e). To further investigate the stability of the material, we carried out XPS characterization of Cu_7S_4/CdS-0.88 catalyst after cyclic. The results showed that the valence state and composition of Cu, Cd and S did not show obvious change, indicating the excellent stability of the catalyst.

3.7 Computational Methods

The structural data of cubic CdS (a=b=c=5.89Å) was obtained from the website of Materials Project, [88], before crystal optimization. A 2×2 CdS (110) with five Cd-S layers was constructed as slab models to represent the non-vacancy CdS (110) model. The vacancy CdS (001) was constructed by removing an S atom on adsorbed Cd−S−Cd sites where lactic acid would interact with the CdS (110) surface. The bottom three layers were fixed to simulate the bulk properties, while the remaining layers and molecules were allowed to relax. The vacuum thickness of all slab models was 15Å. The structure of the lattice acid molecule in the vacuum was calculated using a 15×15×15Å unit cell.

All periodic density functional theory (DFT) calculations were carried out using the Vienna ab initio simulation package (VASP), [89], [90], [91], [92], with the Perdew−Burke−Ernzerhof (PBE) exchange-correlation functional, [93]. A plane wave basis set with an energy cutoff of 400 eV was used. Brillouin zone integration was performed using Γ-only k point mesh and Gaussian smearing of 0.05 eV. Grimme's dispersion correction was employed during each geometry optimization step, [94]. All structures were refined until the Hellman-Feynman forces on each ion were lower than 0.05 eV/Å. The adsorption energies (ΔE_{ads}) of lactic acid on the surface were calculated as follows, (Eq. 4):

$$\Delta E_{ads} = E_{slab+La} - E_{slab} - E_{La} \quad (4)$$

where E_{slab+i}, E_{slab}, and E_{La} are DFT-calculated energies of the adsorption complex, the clean slab, and the gas-phase adsorbate lattice acid molecule, respectively.

The minimum energy surface of the Cu_7S_4/CdS NCs, PLA carrier, and their complexes was calculated through DFT and time-dependent density functional theory (TDDFT) methods at the B3LYP level, [95], [96], in combination with the 6–31 G (d, p) base set of Gaussian 09 software, [97]. This level of theory is sufficiently accurate for a wide variety of dimer systems with non-covalent interactions between drugs and various polymer carriers, [98], [99]. After geometry optimization, the binding energy was calculated as zero-point correction energy (ZPE) at the theoretical level B3LYP/6-31G (d,p) using the following general formula, (Eq. 5):

$$E_{bin} = \left(E_{C_7S_4/CdS/PLA} + ZPE\right) - E_{PLA}\left(E_{C_7S_4/CdS} + ZPE\right) \quad (5)$$

Where E_{PLA} represents the total energy of the pure PLA microparticle, $E_{C7S4/CdS}$ is the total energy of the free Cu_7S_4/CdS molecule, and $E_{Cu7S4/CdS/PLA}$ is the total energy of the complex formed. The solvent effect according to the Polar Continuity Model (PCM), [100], was chosen to evaluate the adsorption mechanism of Cu_7S_4/CdS NCs on PLA in the chloroform phase, based on experimental studies. The quantum molecular

descriptors (QMDs) are used to calculate the physicochemical properties of the interacting systems, (Eq. 6), (Eq. 7), (Eq. 8), (Eq. 9) and (Eq. 10):

$$\mu = -\frac{1}{2}(I + A) \quad (6)$$

$$X = -\mu \quad (7)$$

$$\eta = \frac{1}{2}(I - A) \quad (8)$$

$$S = \frac{1}{2\eta} \quad (9)$$

$$\omega = \frac{\mu^2}{2\eta} \quad (10)$$

According to Koopmans' theorem, the order of ionization potential (I) and electron affinity (A) can be determined by the negative orbital energies of the highest occupied molecular orbital (HOMO), $-E_{HOMO}$, and the lowest unoccupied molecular orbital (LUMO)-E_{LUMO}. In addition, the global softness (S), chemical potential (μ), electronegativity (χ), global hardness (η), and electrophilicity index (ω) are also defined, [101].

Computational results bear certain errors that can arise from the model, assumptions, approximations, and programs. Experimental verification is needed but, in many cases, is not feasible. Typically, one may expect errors of 0.1–0.2 eV, or even more in severe cases, in the DFT-computed energies, which could result in significant errors in energy-sensitive properties such as reaction rate and equilibrium constants, and so on. As a result, relative energies and changing trends are much more consistent. Another problem is that it is not straightforward to compare and analyze the tremendous computed results in the literature since they are calculated using different DFT methods, models, computational parameters, and programs. The development of an efficient and accurate theoretical method for Cu_7S_4/CdS studies is always in high demand, although much progress has been made in the past decades. Error analysis for different theoretical methods is also important, as it may help connect the various calculated results in the literature and provide some standard treatments for specific problems on the Cu_7S_4/CdS surface.

3.8 Binding Energy and Thermodynamic Parameter

In order to determine the binding energy of Cu_7S_4/CdS NCs in interaction with PLA microparticles, three directions were considered. Fig. 17 shows that Cu_7S_4/CdS NCs through its carboxylate group interacts with PLA (State I) via a hydrogen double bond and has an E_{bin} of 0.71 eV by the B3LYP/6-31G** level of theory (maximum energy) in the chloroform environment.

* Figure 17 can be found in the Appendix section.

A model dimer is formed in State I by inter molecular hydrogen bonds, [102]. In a recent study by Soltani et al., [103], it was discovered that the interaction between sulfasalazine and poly (lactic-co-glycolic acid) (PLGA) occurs through a hydrogen double bond, with a binding energy of 0.65 eV. Whereas the E_{bin} value for Cu_7S_4/CdS NCs interacting with PLA in States II and III in order are 0.64 and 0.51 eV by the B3LYP/6-31G** level of theory. The basis set effect on the binding energy in the chloroform environment was calculated. The E_{bin} value in State I, as the most stable state, is found to be 0.58 eV by the B3LYP/6-31 + G** level of theory. The result demonstrated that the E_{bin} value with the basis set 6-31G** was almost similar to the larger basis set 6-31 + G**, [104]. Also, ZPE for Cu_7S_4/CdS NCs interacting with PLA carriers in a chloroform medium was calculated. The ZPE values in States I, II, and III are calculated to be 0.67, 0.61, and 0.46 eV, respectively. Assessment of the binding energy of ZPE indicates that the interaction of Cu_7S_4/CdS NCs with PLA in State I is a chemical interaction in nature. This observation aligns with the computed results obtained from the analysis of thermodynamic parameters. The thermodynamic parameter values for States I, II, and III in the chloroform medium were calculated using B3LYP/6-31G** methods. The obtained values of Gibbs free soluble energy (ΔG_{solv}) and enthalpy (ΔH_{solv}) for State I are +0.5 and 0.05 eV, respectively, and these values in State II are +0.55 and + 0.06 eV and in State III are +0.73 and + 0.21 eV. The amount of difference between ΔG_{solv} and ΔH_{solv} is due to the entropy effect, [105]. Negative values of ΔH_{solv} in State I represent an exothermic process and positive values of ΔG_{solv} represent nonspontaneous interaction between Cu_7S_4/CdS NCs and PLA according to the thermodynamic approach, [106].

The dipole moment (DM) values for pure PLA and Cu_7S_4/CdS NCs molecules are 5.12 and 7.30 Debye, respectively. After Cu_7S_4/CdS NCs interacted with PLA, the DM values in States I, II, and III were 13.98, 8.34, and 7.77 Debye, respectively. The remarkable increase in DM values represents an enhanced interaction of Cu_7S_4/CdS NCs and PLA with non-polar solvents such as chloroform, and would therefore enhance their solubility in physiological media by amplifying in the internal molecular electric field. The presence of electric dipole moments generates a molecular field that induces polarization in neighbouring molecular structures, thereby heightening their reactivity through electrostatic forces. Mulliken

population analysis (MPA) indicates that State I has a strong charge transfer of approximately 0.563 |e| from Cu_7S_4/CdS NCs to PLA compared with States II (0.214 |e|) and III (0.214 |e|). The molecular electrostatic potential (MEP) graphs on PLA and Cu_7S_4/CdS NCs molecules are also displayed in Fig. 18.

* Figure 18 can be found in the Appendix section.

These graphs serve as highly valuable visual representations for observing the locations of reaction sites on the molecular surface in relation to the charge density distribution, [107]. In the three-dimensional MEP plots, the red colour with negative regions and the blue colour with positive regions depict in order the relative accumulation and depletion of electronic charges in a specific order. Therefore, it is clear from the MEP graphs of PLA that the supporter oxygen atoms of the carrier are the most notable sites for attracting nucleophiles. In other words, based on suggestions, it appears that the nitrogen atom of the amine group in Cu_7S_4/CdS NCs could potentially serve as the most favourable site for the electrophilic attack on the oxygen atoms of PLA, depending on the position of the charge density (red colour).

Based on QMD analysis, the η values for the Cu_7S_4/CdS NCs and PLA molecules were 1.81 and 1.34 eV, which varied slightly in States I, II, and III with values of 1.32, 1.34, and 1.34 eV, respectively. Also, states I (4.61 eV), II (4.08 eV), and III (4.14 eV) exhibit various μ values than pure PLA (4.11 eV). This implies that the interactions of the molecules cause notable changes in the electronic properties of the carriers and lead to improved chemical reactivity, [108], [109], [110]. In contrast with the pure PLA (4.11 eV), State I has a higher ω (8.05 eV) than States II (6.21 eV) and III (6.40 eV). Therefore, the ω value represents the electron acceptability of the fragments. During the Cu_7S_4/CdS NCs interaction with PLA, the electrophilicity value of State II was slightly reduced, which confirms that this State readily donates more electrons than the corresponding substances, [111], [112].

3.9 Electronic Properties

It was demonstrated the effects of Cu_7S_4/CdS NCs interaction with PLA carrier on the HOMO and LUMO wavefunctions. The HOMO orbital of the Cu_7S_4/CdS NCs is more focused on the azo bond and only slightly on the carbon and nitrogen atoms. On the other hand, the LUMO orbital focuses more on the azo bond and the phenol/aromatic rings. For PLA, the HOMO and LUMO are concentrated on the atoms of throughout carrier. For Cu_7S_4/CdS NCs interacting with PLA carriers, wave functions for the HOMO and LUMO are displayed in Fig. 16. In State I, the HOMO orbital is more concentrated on the C–C and C-O bonds of the carrier. In contrast, the LUMO orbital is more concentrated on the phenol and aromatic rings of the Cu_7S_4/CdS NCs (Fig. 16). The LUMO orbital, on the other hand, is more focused on the C–C, N bonds of the Cu_7S_4/CdS NCs in States II and III, while the HOMO orbital is more focused on the C–C and C- F- N, and O-H-O bonds of the carrier in both complexes. The HOMO and LUMO energies of the Cu_7S_4/CdS NCs were obtained to be 6.31 and 2.70 eV, respectively, while these energies for the PLA carrier were, in that order, 5.45 and 2.77 eV (Table 1).

* Table 1 can be found in the Appendix section.

Based on the total density of the state, as a consequence of the interaction between Cu_7S_4/CdS NCs and PLA, the energy gap (E_g) value in State II decreased to 2.13 eV, compared to the pure carrier's value of 2.65 eV (Table 1). Comparing States I and III to State I, the energy gap shows minor differences. In State, I, the value of Fermi level (E_F) varies more than in other States. The change of energy gap (ΔE_g) in State II is about 19.62%. Among the interacting complexes, PLA in the State II site is more sensitive to Cu_7S_4/CdS NCs due to the large change in electronic conductivity.

3.10 Artificial Neural Network (ANN) Model Data and Comparison with Research Results

In this study an ANN model linked with an equilibrium for the estimation of H_2(g) production from a photoreactor-DR containing polylactic acid from a real plastic wastes using Cu_7S_4/CdS NCs at different operating conditions such as nanocomposite and pollutant concentrations, pH and photocatalytic time. Based on this method to have comprehensive analysis, variations of the inputs on H_2(g) contents are compared and discussed together.

The ANNs always consist of three layers including (i) input, (ii) hidden, and (iii) output layers. The outputs of a neuron are calculated using Eq. (11):

$$\sigma = f\left(\sum_{j=0}^{n} \omega_j \, x \, X_j\right) \tag{11}$$

where, n: is the input number, x_j: is the j^{th} input to the H_2, ω_j: is the temperature, Cu_7S_4/CdS NCs, and PLA concentrations f: is a non-linear function, respectively. For converting output data between – 1 and + 1, the hyperbolic tangent formula was applied as Eq. (12):

$$\tanh(x) = \frac{2}{1 + e^{-2x}} - 1 \tag{12}$$

During the training process of input and output data set, the network parameters are adjusted to achieve the similar outputs as seen in the training data set. For this purpose, the data were divided into two subsets for

training model and validation purposes. The Pearson correlation coefficient (r^2) and mean standard error (MSE) were computed to evaluate the performance of the developed models according to the following formulas, [113], as Eq. (13) and Eq. (14):

$$r^2 = 1 - \frac{\sum_{i=1}^{N}(y_{pre,i} - y_{exp,i})^2}{\sum_{i=1}^{N}(y_{pre,i} - y_{ave})^2} \quad (13)$$

$$MSE = \frac{1}{N}\sum_{i=1}^{N}\left(\left|y_{pre,i} - y_{exp,i}\right|\right)^2 \quad (14)$$

In order to avoid numerical overflows related to very large or small parameters, all of data were converted to normalized values using as Eq. (15):

$$x_{norm} = 0.8\,x\left(\frac{x_i - x_{min}}{x_{max} - x_{min}}\right) + 0.1 \quad (15)$$

The ANN model was developed to predict the photocatalytic performance of the photoreactor-DR containing polylactic acid from a real plastic wastes using Cu_7S_4/CdS NCs for H_2(g) production. ANN predicts the output of a process given the values of process input and process control variables, [114]. It is often used to model relationships between large sets of varying data. ANN can either feed the results to an operator to make process control adjustments or implement appropriate control adjustments automatically, [114]. Many researchers have used this type of approach with great success and recommended the use of neural network models especially when the exact relationship between inputs and outputs is not known and where strong non-linear relationships exist. It was reported that the real-life anaerobic process for biogas yield is very complex, [115], and non-linear, [116], as well as highly dependent on different substrate characteristics, [117], and various operating conditions such as pH, retention time, carbon/nitrogen ratio, temperature, pressure, agitation rate, etc., [118]. However, one way to understand the relationships between the substrates' characteristics and the optimum biogas yield is through machine learning facilitated by models and equations, [119]. However, determining an exact mathematical model is rigorous because the relationships are very complex and highly non-linear, [114].

H_2(g) production yields detected from ANN Model and experimental studies in a photoreactor-DR were compared for H_2(g) production yields versus increasing time, nanocomposite and pollutant concentrations and pH values. The results were given in Figures 19, 20, 21 and 22 with y error bars.

* Figure 19 can be found in the Appendix section.

* Figure 20 can be found in the Appendix section.

* Figure 21 can be found in the Appendix section.

* Figure 22 can be found in the Appendix section.

The data showed that the experimental data can be defined with ANN model. Very similar results were detected from this model and experimental results. The value of R^2 for the ANN model was found to be around 0.98 and 0.99 (data not shown).

The ANN was an excellent model because of the lowest error and the highest coefficient values. The obtained results indicated that the simulation model based on the ANN is very practical.

3.11 Reusability of Cu_7S_4/CdS NCs

In addition to photocatalytic performance, nanocomposites must possess a recyclable character, which is a key factor in evaluating their stability in practical applications. Due to their mechanical strength and stability, Cu_7S_4/CdS NCs materials can be regenerated by following an appropriate desorption procedure. Thus, better acid–alkaline resistance of Cu_7S_4/CdS NCs assists them in retaining their original photocatalytic efficiency. For example, a removal efficiency greater than 98% for up to 40 regeneration cycles was obtained by the aforementioned nanocomposite (Table 2). The PLA photocatalytic capacity remained stable for 30 cycles as 99%, while the PLA uptake and photodegradation yields of PLA decreased slightly to 98% after 35 cycles. As a result, 98% regeneration was achieved for 50 mg/l Cu_7S_4/CdS NCs during 10 mg/l PLA degradation (Table 2).

* Table 2 can be found in the Appendix section.

4 Conclusions

Maximum 99.69% H_2(g) production efficiency was obtained after photocatayltic degradation of real plastic wastewater containing 10 mg/l polylactic acid using 50 mg/l Cu_7S_4/CdS nanocomposite concentration at pH=7.0, after 240 min photooxidation time under 300 W UV-vis light and at 25°C, respectively. The reusability of Cu_7S_4/CdS NCs was applied during 40 cycles. The PLA photocatalytic capacity remained stable for 30 cycles as 99%, while the PLA uptake and photodegradation yields of PLA decreased slightly to 98% after 35 cycles. As a result, 98% regeneration was achieved for 50 mg/l Cu_7S_4/CdS NCs during 10 mg/l PLA degradation.

Z-scheme Cu_7S_4/CdS photocatalysts were success fully prepared through a solution-mediated cation exchange process. By controlling the exchange time, the well-defined heterostructures with various Cu_7S_4/CdS ratios are easily obtained. The single-

nanoparticle impact studies demonstrate that the Cu_7S_4/CdS ratio are critical for electrons accumulation on Cu_7S_4 domain. These studies improved the understanding of how the role of Cu_7S_4/CdS ratio in photocatalyst influences the reactivity and the stability of catalysts. Utilizing the hot electrons and holes, the hybrid scan effectively promotes H_2 production from polylactic acid reforming.

The investigation of the interaction between Cu_7S_4/CdS NCs and PLA in the chloroform phase was carried out using DFT and TDDFT. The thermodynamic parameters and binding energies suggest that the interaction between Cu_7S_4/CdS NCs and PLA improve the dipole moment and solubility of the complexes especially via hydrogen double bond. The MEP graphs show the chemical reactivity sites of the oxygen atoms of the carrier molecule (PLA). The QMD analysis exhibits significant changes in the electronic properties of the complexes with respect to pure PLA and leads to improved chemical reactivity. The change in the energy gap of the complexes shows the interaction between the Cu_7S_4/CdS NCs and PLA. The UV–vis analysis and IR spectroscopy study indicate aligns well with the experimental findings. There were no noticeable differences between the optimized complexes and the experimental structure. Based on this study, the findings suggest that PLA has the capability to serve as a carrier for Cu_7S_4/CdS NCs.

High H_2(g) production efficiency was obtained from a real plastic wastes containing PLA using Cu_7S_4/CdS nanocomposite as a photocatalyst. The experimental data match with the data estimated from ANN model. Photocatalytic degradation process is very effective, easy to apply, and environmentally friendly method for the removal of plastic and microplastic wastes from environmental areas.

Acknowledgement:
Experimental analyzes in this study were performed at the Laboratories of the Canada Research Center, Ottawa, Canada. The authors would like to thank this body for providing financial support.

References:

[1] J. M. Garcia, M. L. Robertson, The Future of Plastics Recycling, *Science*, Vol.358, 2017, pp. 870−872.

[2] R. Geyer, J. R. Jambeck, K. L. Law, Production, Use, and Fate of All Plastics ever Made, Science Advances, Vol.3, 2017, No.e1700782.

[3] E. MacArthur, Beyond Plastic Waste, *Science*, Vol.358, 2017, 843.

[4] A. Cozar, F. Echevarría, J. I. Gonzalez-Gordillo, X. Irigoien, B. Úbeda, S. Hernandez-Leon, A. T. Palma, S. Navarro, J. García-de Lomas, A. Ruiz, M. L. Fernandez-de-Puelles, C. M. Duarte, Plastic Debris in the Open Ocean, *Proceedings of the National Academy of Sciences of the United States of America*, Vol.111, 2014, pp. 10239−10244.

[5] K. L. Law, R. C. Thompson, Microplastics in the Seas, *Science*, Vol.345, 2014, pp. 144−145.

[6] A. L. Andrady, *Persistence of Plastic Litter in the Oceans*, In Marine Anthropogenic Litter; Springer International Publishing: Cham., pp. 57−72, 2015.

[7] M. Kosuth, S. A. Mason, E. V. Wattenberg, Anthropogenic Contamination of Tap Water, Beer, and Sea Salt, *PLoS One*, Vol.13, No.e0194970, 2018.

[8] S. A. Mason, V. G., Welch, J. Neratko, Synthetic Polymer Contamination in Bottled Water, *Frontiers in Chemistry*, Vol.6, 2018, Article 407.

[9] M. Pivokonsky, L. Cermakova, K. Novotna, P. Peer, T. Cajthaml, V. Janda, Occurrence of Microplastics in Raw and Treated Drinking Water, *Science of the Total Environment*, Vol.643, 2018, pp. 1644−1651.

[10] J. Lunt, Large-Scale Production, Properties and Commercial Applications of Polylactic acid Polymers, *Polymer Degradation and Stability*, Vol.59, 1998, pp. 145–152.

[11] D. Maga, M. Hiebel, N. Thonemann, Life Cycle Assessment of Recycling Options for Polylactic Acid, *Resources, Conservation and Recycling*, Vol.149, 2019, pp. 86–96.

[12] M. L. D. Lorenzo, R. Androsch, *Applications of Poly(Lactic Acid) in Commodities and Specialties*, 1st ed.; Springer: Berlin/Heidelberg, Germany, 2018, pp. 1–16.

[13] *Bioplastics Market Development Update 2019*, Available online: https://docs.european-bioplastics.org/conference/Report_Bioplastics_Market_Data_2020_short_version.pdf (accessed on 24 November 2025).

[14] *M.* Hong, Y. X. Chen, Chemically Recyclable Polymers: A Circular Economy Approach to Sustainability, *Green Chemistry*, Vol.19, 2017, pp. 3692–3706.

[15] *V.* Rossi, N. Cleeve-Edwards, L. Lundquist, U. Schenker, C. Dubois, S. Humbert, O. Jolliet, Life Cycle Assessment of End-of-Life Options for Two Biodegradable Packaging Materials: Sound Application of the European Waste Hierarchy, *Journal of Cleaner Production*, Vol.86, 2015, pp. 132–145.

[16] B. Laycock, M. Nikolic, J. M. Colwell, E. Gauthier, P. Halley, S. Bottle, G. George, Lifetime Prediction of Biodegradable Polymers, *Progress in Polymer Science*, Vol.71, 2017, pp. 144–189.

[17] C. Sun, S. Wei, H. Tan, Y. Huang, Y. Zhang, Progress in Upcycling Polylactic Acid Waste as an

Alternative Carbon Source: A Review, Chemical Engineering Journal, Vol.446, 2022, 136881.

[18] A. M. Cristina, F. Sara, G. Fausto, P. Vincenzo, S. Rocchina, V. Claudio, Degradation of Post-Consumer PLA: Hydrolysis of Polymeric Matrix and Oligomers Stabilization in Aqueous Phase, *Journal of Polymers and the Environment,* Vol.26, 2018, pp. 4396–4404.

[19] M. N. Siddiqui, L. Kolokotsiou, E. Vouvoudi, H. H. Redhwi, A. A. Al-Arfaj, D. S. Achilias, Depolymerization of PLA by Phase Transfer Catalysed Alkaline Hydrolysis in a Microwave Reactor, Journal of Polymers and the Environment, Vol.28, 2020, pp. 1664–1672.

[20] M. Garg, S. R. White, N. R. Sottos, Rapid Degradation of Poly(lactic acid) with Organometallic Catalysts, *ACS Applied Materials & Interfaces,* Vol.11, 2019, pp. 46226–46232.

[21] C. Sun, C. Li, H. Tan, Y. Zhang, Synergistic Effects of Wood Fiber and Polylactic Acid during Co-Pyrolysis Using TG-FTIR-MS and Py-GC/MS, *Energy Conversion and Management*, Vol.202, 2019, 112212.

[22] P. McKeown, M. Kamran, M. G. Davidson, M. D. Jones, L. A. Román-Ramírez, J. Wood, Organocatalysis for Versatile Polymer Degradation, *Green Chemistry*, Vol.22, 2020, pp. 3721–3726.

[23] P. Majgaonkar, R. Hanich, F. Malz, R. Brüll, Chemical Recycling of Post-Consumer PLA Waste for Sustainable Production of Ethyl Lactate, *Chemical Engineering Journal*, Vol.423, 2021, 129952.

[24] K. Saeaung, N. Phusunti, W. Phetwarotai, S. Assabumrungrat, B. Cheirsilp, Catalytic Pyrolysis of Petroleum-Based and Biodegradable Plastic Waste to Obtain High-Value Chemicals, *Waste Management*, Vol.127, 2021, pp. 101–111.

[25] J. Xu, K. Zhou, J. Fu, Z. Tan, L. Qin, P. Duan, Y. Xu, S. Kang, Near-Zero-Waste Hydrogenolysis of Poly(lactic acid) to Biofuel, *Fuel*, Vol.334, 2023, 126609.

[26] S. Tian, Y. Jiao, Z. Gao, Y. Xu, L. Fu, H. Fu, W. Zhou, C. Hu, G. Liu, M. Wang, D. Ma, Catalytic Amination of Polylactic Acid to Alanine, *Journal of the American Chemical Society*, Vol.143, No.40, 2021, pp. 16358–16363.

[27] J. M. Ogden, Prospects for Building a Hydrogen Energy Infrastructure, *Annual Review of Environment and Resources*, Vol.24, No.1, 1999, pp. 227-279.

[28] W. G. Colella, D. M. Golden, M. Z. Jacobson, Cleaning the Air and Improving Health with Hydrogen Fuel-Cell Vehicles, *Science,* Vol.308, No.5790, 2005, pp. 1901-1905.

[29] J. Xu, J. Cui, C. Guo, Z. Zhao, R. Jiang, S. Xu, Z. Zhuang, Y. Huang, L. Wang, Y. Li, Ultrasmall Cu_7S_4@MoS_2 Hetero-Nanoframes with Abundant Active Edge Sites for Ultrahigh-Performance Hydrogen Evolution, *Angewandte Chemie International Edition*, Vol.55, No.22, 2016a, pp. 6502-6505.

[30] Y. Xu, Y. Huang, B. Zhang, Rational Design of Semiconductor-Based Photocatalysts for Advanced Photocatalytic Hydrogen Production: the Case of Cadmium Chalcogenides, *Inorganic Chemistry Frontiers*, Vol.3, 2016b, pp. 591-615.

[31] D. N. Chirdon, Y. Wu, Hydrogen Evolution: Not Living on the Edge, *Nature Energy*, Vol.2, 2017, Article number:17132.

[32] A. Kudo, Y. Miseki, Heterogeneous Photocatalyst Materials for Water Splitting, *Chemical Society Reviews*, Vol.38, 2009, pp. 253-278.

[33] Y. Chao, P. Zhou, N. Li, J. Lai, Y. Yang, Y. Zhang, Y. Tang, W. Yang, Y. Du, D. Su, Y. Tan, S. Guo, Ultrathin Visible-Light-Driven Mo Incorporating In_2O_3–$ZnIn_2Se_4$ Z-Scheme Nanosheet Photocatalysts, *Advanced Materials*, Vol.31, No.5, 2019, 1807226.

[34] T. Hu, K. Dai, J. Zhang, S. Chen, Noble-Metal-Free Ni_2P Modified Step-Scheme SnNb2O6/CdS-Diethylenetriamine for Photocatalytic Hydrogen Production under Broadband Light Irradiation, *Applied Catalysis B: Environmental*, Vol.269, 2020, 118844.

[35] X. Liu, H. Zhuang, Recent Progresses in Photocatalytic Hydrogen Production: Design and Construction of Ni-Based Cocatalysts, *International Journal of Energy Research*, Vol.45, No.2, 2021, pp. 1480-1495.

[36] P. Zhang, J. Wang, Y. Li, L. Jiang, Z. Wang, G. Zhang, Non-Noble-Metallic Cocatalyst Ni_2P Nanoparticles Modified Graphite-Like Carbonitride with Enhanced Photocatalytic Hydrogen Evolution under Visible Light Irradiation, *Acta Physico-Chimica Sinica*, Vol.37, No.8, 2021, 2009102.

[37] T. Hisatomi, J. Kubota, K. Domen, Recent Advances in Semiconductors for Photocatalytic and Photoelectrochemical Water Splitting, *Chemical Society Reviews*, Vol.43, No.22, 2014, pp. 7520-7535.

[38] C. Zhang, C. Yan, Z. Xue, W. Yu, Y. Xie, T. Wang, Shape-Controlled Synthesis of High-Quality Cu_7S_4 Nanocrystals for Efficient Light-Induced Water Evaporation, *Small*, 2016a;12(38):5320-5328.

[39] P. Zhang, T. Wang, X. Chang, J. Gong, Effective Charge Carrier Utilization in Photocatalytic Conversions, *Accounts of Chemical Research*, Vol.49, No.5, 2016b, pp. 911-921.

[40] X. Y. Cai, M. S. Zhu, O. A. Elbanna, M. Fujitsuka, S. Kim, L. Mao, J. Y. Zhang, T. Majima, Au Nanorod Photosensitized $La_2Ti_2O_7$ Nanosteps: Successive Surface Heterojunctions Boosting Visible to Near-Infrared Photocatalytic H_2 Evolution, *ACS Catalysis*, Vol.8, 2018, pp. 122–131.

[41] X.-Y. Fu, Z.-Q. Wei, S. Xu, X. Lin, S. Hou, F.-X. Xiao, Maneuvering Intrinsic Instability of Metal Nanoclusters for Boosted Solar-Powered Hydrogen Production, *Journal of Physical Chemistry Letters*, Vol.11, 2020, pp. 9138-9143.

[42] Y.-B. Li, T. Li, X.-C. Dai, M.-H. Huang, S. Hou, X.-Y. Fu, Z.-Q. Wei, Y. He, G. Xiao, F.-X. Xiao, Precise Tuning of Coordination Positions for Transition-Metal Ions via Layer-by-Layer Assembly to Enhance Solar Hydrogen Production, *ACS Applied Materials & Interfaces*, Vol.12, No.4, 2020, pp. 4373-4384.

[43] S.-C. Zhu, Z.-C. Wang, B. Tang, H. Liang, B.-J. Liu, S. Li, Z. Chen, N.-C. Cheng, F.-X. Xiao, Progressively Stimulating Carrier Motion Over Transient Metal Chalcogenide Quantum Dots Towards Solar-to-Hydrogen Conversion, *Journal of Materials Chemistry A*, Vol.10, 2022, pp. 11926-11937.

[44] *International Energy Agency (IEA), Tracking Clean Energy Progress 2015: Energy Technology Perspectives 2015*, Excerpt IEA Input to the Clean Energy Ministerial; Paris, 2015.

[45] P. L. Spath, M. K. Mann, *Life Cycle Assessment of Hydrogen Production via Natural Gas Steam Reforming, Technical Report*, Golden, National Renewable Energy Laboratory, NREL/TP-570-27637, U.S. Department of Energy Office of Scientific and Technical Information (OSTIGOV), pp. 1-31, 2001.

[46] W.-T. Chen, K. Jin, N.-H. L. Wang, Use of Supercritical Water for the Liquefaction of Polypropylene into Oil, *ACS Sustainable Chemistry & Engineering*, Vol.7, No.4, 2019, pp. 3749−3758.

[47] D. W. Wakerley, M. F. Kuehnel, K. L. Orchard, K. H. Ly, T. E. Rosser, E. Reisner, Solar-Driven Reforming of Lignocellulose to H_2 with a CdS/CdO_x Photocatalyst, Nature Energy, Vol.2, 2017, Article number:17021.

[48] B. Ohtani, S. Adzuma, S. Nishimoto, T. Kagiya, Photocatalytic Degradation of Polyethylene Film by Incorporated Extra Fine Particles of Titanium Dioxide, *Polymer Degradation and Stability*, Vol.35, 1992, pp. 53−60.

[49] S. Horikoshi, N. Serpone, Y. Hisamatsu, H. Hidaka, Photocatalyzed Degradation of Polymers in Aqueous Semiconductor Suspensions. 3. Photooxidation of a Solid Polymer: TiO_2-Blended Poly(vinyl chloride) Film, *American Chemical Society (ACS) in Environmental Science & Technology*, Vol.32, No.24, 1998, pp. 4010− 4016.

[50] T. S. Tofa, K. L. Kunjali, S. Paul, J. Dutta, Visible Light Photocatalytic Degradation of Microplastic Residues with Zinc Oxide Nanorods, *Environmental Chemistry Letters*, Vol.17, 2019, pp. 1341−1346.

[51] M. F. Kuehnel, E. Reisner, Solar Hydrogen Generation from Lignocellulose, *Angewandte Chemie International Edition*, Vol.57, 2018, pp. 3290−3296.

[52] X. Zhou, T. L. Shelton, Z. Xia, Y. Ma, Turbostratic Carbon Nitride Enhances the Performance and Stability of Cadmium Sulfide Nanorod Hydrogen Evolution Photocatalysts, *Inorganic Chemistry Frontiers*, Vol.4, 2017, pp. 1923-1929.

[53] C. Wolff, P. Frischmann, M. Schulze, B. J. Bohn, R. Wein, P. Livadas, M. T. Carlson, F. Jäckel, J. Feldmann, F. Würthner, J. K. Stolarczyk, All-in-One Visible-Light-Driven Water Splitting by Combining Nanoparticulate and Molecular Co-Catalysts on CdS Nanorods, *Nature Energy*, Vol.3, No.10, 2018, 862.

[54] R. Shen, D. Ren, Y. Ding, Y. Guan, Y. H. Ng, P. Zhang, X. Li, Nanostructured CdS for Efficient Photocatalytic H_2 Evolution: A Review, *Science China Materials*, Vol.63, No.11, 2020a, pp. 2153-2188.

[55] R. Shen, L. Zhang, X. Chen, M. Jaroniec, N. Li, X. Li, Integrating 2D/2D CdS/α-Fe_2O_3 Ultrathin Bilayer Z-Scheme Heterojunction with Metallic β-NiS Nanosheet-Based Ohmic-Junction for Efficient Photocatalytic H_2 Evolution, *Applied Catalysis B-Environment and Energy*, Vol.266, 2020b, 118619.

[56] D. W. Wakerley, M. F. Kuehnel, K. L. Orchard, K. H. Ly, T. E. Rosser, E. Reisner, Solar-Driven Reforming of Lignocellulose to H_2 with a CdS/CdO_x Photocatalyst, *Nature Energy*, Vol.2, 2017, 17021.

[57] T. Uekert, M. F. Kuehnel, D. W. Wakerley, E. Reisner, Plastic Waste as a Feedstock for Solar-Driven H_2 Generation, *Energy & Environmental Science*, Vol.11, 2018, pp. 2853−2857.

[58] D. Ren, R. Shen, Z. Jiang, X. Lu, X. Li, Highly Efficient Visible-Light Photocatalytic H_2 Evolution Over 2D–2D CdS/Cu_7S_4 Layered Heterojunctions, *Chinese Journal of Catalysis*, Vol.41, No.1, 2020, pp. 31-40.

[59] R. C. Shen, Y. N. Ding, S. B. Li, P. Zhang, Q. J. Xiang, Y. H. Ng, X. Li, Constructing Low-Cost Ni_3C/twin-Crystal $Zn_{0.5}Cd_{0.5}S$ Heterojunction/Homojunction Nanohybrids for Efficient Photocatalytic H2 Evolution, *Chinese*

Journal of Catalysis, Vol.42, No.1, 2021, pp. 25–36.

[60] Y. Chen, S. Zhao, X. Wang, Q. Peng, R. Lin, Y. Wang, R. Shen, X. Cao, L. Zhang, G. Zhou, J. Li, A. Xia, Y. Li, Synergetic Integration of Cu1.94S–ZnxCd1–xS Heteronanorods for Enhanced Visible-Light-Driven Photocatalytic Hydrogen Production, *Journal of the American Chemical Society*, Vol.138, No.13, 2016, pp. 4286–4289.

[61] P. Bhavani, D. P. Kumar, H. S. Shim, P. Rangappa, M. Gopannagari, D. A. Reddy, J. K. Song, T. K. Kim, In Situ Addition of Ni Salt onto a Skeletal Cu_7S_4 Integrated CdS Nanorod Photocatalyst for Efficient Production of H_2 under Solar Light Irradiation, *Catalysis Science & Technology*, Vol.10, 2020, ppp. 3542-3551.

[62] J. Low, C. Jiang, B. Cheng, S. Wageh, A. A. Al-Ghamdi, J. Yu, A Review of Direct Z-Scheme Photocatalysts, *Small Methods*, Vol.1, No.5, 2017, 1700080.

[63] B. Qiu, Q. Zhu, M. Du, L. Fan, M. Xing, J. Zhang, Efficient Solar Light Harvesting CdS/Co_9S_8 Hollow Cubes for Z-Scheme Photocatalytic Water Splitting, *Angewandte Chemie International Edition*, Vol.56, No.10, 2017, pp. 2684-2688.

[64] Y. Chen, S. Zhao, X. Wang, Q. Peng, R. Lin, Y. Wang, R. Shen, X. Cao, L. Zhang, G. Zhou, J. Li, A. Xia, Y. Li, Synergetic Integration of Cu1.94S–ZnxCd1–xS Heteronanorods for Enhanced Visible-Light-Driven Photocatalytic Hydrogen Production, *Journal of the American Chemical Society*, Vol.138, No.13, 2016, pp. 4286–4289.

[65] Z. Lian, M. Sakamoto, H. Matsunaga, J. J. M. Vequizo, A. Yamakata, M. Haruta, H. Kurata, W. Ota, T. Sato, T. Teranishi, Near Infrared Light Induced Plasmonic Hot Hole Transfer at a Nano-Heterointerface, *Nature Communications,* Vol.9, 2018, Article number:2314.

[66] A. V. Puga, Photocatalytic Production of Hydrogen from Biomass-Derived Feedstocks, *Coordination Chemistry Reviews*, Vol.315, 2016, pp. 1−66.

[67] Y. Pellegrin, F. Odobel, Sacrificial Electron Donor Reagents for Solar Fuel Production, *Comptes Rendus Chimie*, Vol.20, 2017, pp. 283−295.

[68] T. Kawai, T. Sakata, Photocatalytic Hydrogen Production from Water by the Decomposition of Poly-vinylchloride, Protein, Algae, Dead Insects, and Excrement, *Chemistry Letters*, Vol.10, 1981, pp. 81−84.

[69] L. Mi, Y. Chen, W. Wei, W. Chen, H. Hou, Z. Zheng, Large-Scale Urchin-Like Micro/Nano-Structured NiS: Controlled Synthesis, Cation Exchange and Lithium-Ion Battery Applications, *RSC Advances*, Vol.3, No.38, 2013a, pp. 17431-17439.

[70] L. Mi, W. Wei, Z. Zheng, Y. Gao, Y. Liu, W. Chen, X. Guan, Tunable Properties Induced by Ion Exchange in Multilayer Intertwined CuS Microflowers with Hierarchal Structures, *Nanoscale*, Vol.5, 2013b, pp. 6589-6598.

[71] W. Wei, J. Wu, S. Cui, Y. Zhao, W. Chen, L. Mi, α-$Ni(OH)_2$/$NiS_{1.97}$ Heterojunction Composites with Excellent Ion and Electron Transport Properties for Advanced Supercapacitors, *Nanoscale*, Vol.11, 2019, pp. 6243-6253.

[72] W. Wei, W. Chen, L. Mi, J. Xu, J. Zhang, High-Rate Performance Aqueous-Based Supercapacitors at −30°C Driven by Novel 1D $Ni(OH)_2$ Nanorods and a Two-Solute Electrolyte, *Journal of Materials Chemistry A*, Vol.9, 2021, pp. 23860-23872.

[73] W. Wei, J. Xu, W. Chen, L. Mi, J. Zhang, A Review of Sodium Chloride-Based Electrolytes and Materials for Electrochemical Energy Technology, *Journal of Materials Chemistry A*, Vol.10, 2022, pp. 2637-2671.

[74] J. L. Fenton, B. C. Steimle, R. E. Schaak, Tunable Intraparticle Frameworks for Creating Complex Heterostructured Nanoparticle Libraries, *Science*, Vol.360, No.6388, 2018, pp. 513–517.

[75] T. Uekert, M. F. Kuehnel, D. W. Wakerley, E. Reisner, Plastic Waste as a Feedstock for Solar-Driven H_2 Generation, *Energy & Environmental Science*, Vol.11, No.10, 2018, pp. 2853-2857.

[76] V. N. Emel'yanenko, S. P. Verevkin, C. Schick, E. N. Stepurko, G. N. Roganov, M. K. Georgieva, The Thermodynamic Properties of S-Lactic Acid, Russian Journal of Physical Chemistry A, Vol.84, 2010, pp. 1491–1497.

[77] *NIST Chemistry WebBook. 1,2-Ethanediol* https://webbook.nist.gov/cgi/cbook.cgi?ID=C107211&Mask=2 (accessed 24 November, 2025).

[78] J. H. Zar, Biostatistical Analysis, Prentice-Hall, Englewood Cliffs, 1984.

[79] Statgraphics Centurion XV, Sofware, StatPoint Inc, Statgraphics Centurion XV, Herndon, VA, USA, 2005.

[80] B. Sadtler, D. O. Demchenko, H. Zheng, S. M. Hughes, M. G. Merkle, U. Dahmen, L.-W. Wang, A. P. Alivisatos, Selective Facet Reactivity during Cation Exchange in Cadmium Sulfide Nanorods, *Journal of the American Chemical Society*, Vol.131, No.14 2009, pp. 5285-5293.

[81] K. R. Gopidas, M. Bohorquez, P. V. Kamat, Photophysical and Photochemical Aspects of Coupled Semiconductors: Charge-Transfer Processes in Colloidal Cadmium Sulfide-Titania and Cadmium Sulfide-Silver(I) Iodide Systems, *Journal of Physical Chemistry*, Vol.94, No.16, 1990, pp. 6435–6440.

[82] M. Haase, H. Weller, A. Henglein, Photochemistry of Colloidal Semiconductors. 26. Photoelectron Emission from Cadmium Sulfide Particles and Related Chemical Effects, *The Journal of Physical Chemistry*, Vol.92, No.16, 1988, pp. 4706–4712.

[83] S. M. Oja, D. A. Robinson, N. J. Vitti, M. A. Edwards, Y. Liu, H. S. White, B. Zhang, Observation of Multipeak Collision Behavior during the Electro-Oxidation of Single Ag Nanoparticles, *Journal of the American Chemical Society*, Vol.139, No.2, 2017, pp. 708–718.

[84] Zhou M.; Yu Y.; Hu K.; Xin H. L.; Mirkin M. V. Collisions of Ir Oxide Nanoparticles with Carbon Nanopipettes: Experiments with One Nanoparticle. *Analytical Chemistry*, Vol.89, No.5, 2017, pp. 2880–2885.

[85] Z.-W. Zhang, Q.-H. Li, X.-Q. Qiao, D. Hou, D.-S. Li, One-pot Hydrothermal Synthesis of Willow Branch-shaped MoS_2/CdS Heterojunctions for Photocatalytic H_2 Production under Visible Light Irradiation, Chinese Journal of Catalysis, Vol.40, No.3, 2019, pp. 371-379.

[86] Z. Liang, R. Shen, Y. H. Ng, P. Zhang, Q. Xiang, X. Li, A Review on 2D MoS_2 Cocatalysts in Photocatalytic H_2 Production, Journal of Materials Science & Technology, Vol.56, 2020, pp. 89-121.

[87] D. Ren, Z. Liang, Y. H. Ng, P. Zhang, Q. Xiang, X. Li, Strongly Coupled 2D-2D Nanojunctions between P-Doped Ni_2S (Ni_2SP) Cocatalysts and CdS Nanosheets for Efficient Photocatalytic H_2 Evolution, Chemical Engineering Journal, Vol.390, 2020, 124496.

[88] A. Jain S. P. Ong, G. Hautier, W. Chen, W. D. Richards, S. Dacek, S. Cholia, D. Gunter, D. Skinner, G. Ceder, K. A. Persson, Commentary: The Materials Project: A Materials Genome Approach to Accelerating Materials Innovation, *APL Materials*, Vol.1, 2013, 011002.

[89] G. Kresse, J. Hafner, Ab Initio Molecular Dynamics for Open-Shell Transition Metals, *Physical Review B: Condensed Matter and Materials Physics*, Vol.48, 1993, pp. 13115–13118.

[90] G. Kresse, J. Hafner, Ab Initio Molecular-Dynamics Simulation of the Liquid-Metal-Amorphous-Semiconductor Transition in Germanium, *Physical Review B: Condensed Matter and Materials Physics*, Vol.49, 1994, pp. 14251–14269.

[91] G. Kresse, J. Furthmuller, Efficiency of Ab-Initio Total Energy Calculations for Metals and Semiconductors using a Plane-Wave Basis Set, *Computational Materials Science*, Vol.6,1996, pp. 15–50.

[92] G. Kresse, J. Furthmuller, Efficient Iterative Schemes for Ab Initio Total-Energy Calculations using a Plane-Wave Basis Set, *Physical Review B: Condensed Matter and Materials Physics*, Vol.54, 1996, pp. 11169–11186.

[93] J. P. Perdew, K. Burke, M. Ernzerhof, Generalized Gradient Approximation Made Simple, *Physical Review Letters*, Vol.77, 1996, pp. 3865–3868.

[94] S. Grimme, Semiempirical GGA-Type Density Functional Constructed with a Long-Range Dispersion Correction, *Journal of Computational Chemistry*, Vol.27, 2006, pp. 1787–1799.

[95] A. D. Becke, Density-Functional Thermochemistry. III. The Role of Exact Exchange, *Journal of Chemical Physics*, Vol.98, 1993, pp. 5648–5652.

[96] C. Lee, W. Yang, R. G. Parr, Development of the Colle-Salvetti correlation-energy formula into a functional of the electron density, *Physical Review B*, Vol.37, 1988, pp. 785–789.

[97] D. 01 M. J. Frisch, G. W. Trucks, H. B. Schlegel, G. E. Scuseria, M. A. Robb, J. R. Cheeseman, G. Scalmani, V. Barone, B. Mennucci, G. A. Petersson, H. Nakatsuji, M. Caricato, X. Li, H. P. Hratchian, A. F. Izmaylov, J. Bloino, G. Zheng, J. L. Sonnenberg, M. Hada, M. Ehara, K. Toyota, R. Fukuda, J. Hasegawa, M. Ishida, T. Nakajima, Y. Honda, O. Kitao, H. Nakai, T. Vreven, J. A. Montgomery Jr., J. E. Peralta, F. Ogliaro, M. Bearpark, J. J. Heyd, E. Brothers, K. N. Kudin, V. N. Staroverov, R. Kobayashi, J. Normand, K. Raghavachari, A. Rendell, J. C. Burant, S. S. Iyengar, J. Tomasi, M. Cossi, N. Rega, J.M. Millam, M. Klene, J. E. Knox, J. B. Cross, V. Bakken, C. Adamo, J. Jaramillo, R. Gomperts, R. E. Stratmann, O. Yazyev, A. J. Austin, R. Cammi, C. Pomelli, J. W. Ochterski, R. L. Martin, K. Morokuma, V. G. Zakrzewski, G. A. Voth, P. Salvador, J. J. Dannenberg, S. Dapprich, A. D. Daniels, O. Farkas, J. B. Foresman, J. V. Ortiz, J. Cioslowski, D. J. Fox, *Gaussian 09, Revision, Gaussian*, Inc., Wallingford CT, 2009.

[98] H. Tsuji, Poly (lactic acid) Stereocomplexes: A Decade of Progress, *Advanced Drug Delivery Reviews*, Vol.107, 2016, pp. 97–135.

[99] K. Yu, J. Ni, H. Zhou, X. Wang, J. Mi, Effects of In-Situ Crystallization on Poly (lactic acid) Microcellular Foaming: Density Functional Theory and Experiment, *Polymer*, Vol.200, 2020, 122539.

[100] A. V. Marenich, C. J. Cramer, D. G. Truhlar, Universal Solvation Model Based on Solute Electron Density and on a Continuum Model of the Solvent Defined by the Bulk Dielectric Constant and Atomic Surface Tensions, *The Journal of Physical Chemistry B*, Vol.113, No.18, 2009, pp. 6378–6396.

[101] M. Karelson, V. S. Lobanov, A. R. Katritzky, Quantum-Chemical Descriptors in QSAR/QSPR Studies, *Chemical Reviews*, Vol.96, No.3, 1996, pp. 1027–1044.

[102] E. Ibrahim, K. Taylor, S. Ahmed, A. Mahmoud, K. Lozano, Centrifugally Spun Poly (D, L-lactic acid)-alginate Composite Microbeads for Drug Delivery and Tissue Engineering, *International Journal of Biological Macromolecules*, Vol.237, 2023, 123743.

[103] M. Hajian, V. Erfani-Moghadam, M. Sheikh Arabi, A. Soltani, M. Shahbazi, A Comparison between Optimized PLGA and CS-Alg-PLGA Microspheres for Long- Lasting Release of Glatiramer Acetate, *Journal of Drug Delivery Science and Technology*, Vol.82, 2023, 104355.

[104] A. Soltani, V. Erfani-Moghadam, A. Yahyazadeh, N. O. Mahmoodi, Synthesis, Spectroscopic Characterization, Molecular Docking, as well as In Vitro Cytotoxicity of Calcium-Sulfasalazine Complex, *Journal of Molecular Structure*, Vol.1267, 2022, 133568.

[105] R. S. Fernandes, A. Tiwari, S. Kanungo, N. Dey, Formation of Stable Naphthalenediimide Radical Anion: Substituent-Directed Synergistic Effects of Hydrogen Bonding and Charge Transfer Interactions on Chromogenic Response Towards Hydrazine, *Journal of Molecular Liquids*, Vol.387, 2023, 122238.

[106] M. Aghaei, V. Erfani-Moghadam, L. Daneshmandi, A. Soltani, N. Abdolahi, M. Cordani, A. Yahyazadeh, S. Moazen Rad, S. Tavassoli, H. Balakheyli, Non-Ionic Surfactant Vesicles as Novel Delivery Systems for Sulfasalazine: Evaluation of the Physicochemical and Cytotoxic Properties, *Journal of Molecular Structure*, Vol.1230, 2021, 129874.

[107] M. Muzomwe, G. Maes, O. Emile Kasende, Theoretical DFT(B3LYP)/6-31+G(d) Study on the Prediction of the Preferred Interaction Site of 3-Methyl-4-pyri midone with Different Proton Donors, *Natural Science*, Vol.4, 2012, pp. 286–297.

[108] R. Guo, Q. Liu, W. Wang, R. Tayebee, F. Mollania, Boron Nitride Nanostructures as Effective Adsorbents for Melphalan Anti-ovarian Cancer Drug. Preliminary MTT Assay and In Vitro Cellular Toxicity, *Journal of Molecular Liquids*, Vol.325, 2021, 114798.

[109] M. Aghaei, M. Ramezanitaghartapeh, M. Javan, M. S. Hoseininezhad-Namin, H. Mirzaei, A. Shokuhi Rad, A. Soltani, S. Sedighi, A. Ng Kay Lup, V. Khori, J. Peter, Mahon b, F. Heidari, Investigations of Adsorption Behavior and Anti-inflammatory Activity of Glycine Functionalized $Al_{12}N_{12}$ and $Al_{12}ON_{11}$ Fullerene like Cages, Spectrochimica Acta Part A: Molecular and Biomolecular Spectroscopy, Vol.246, 2021, 119023.

[110] M. R. Hossain, M. M. Hasan, M. Nishat, N.-E.-Ashrafi, F. Ahmed, T. Ferdous, M. A. Hossain, DFT and QTAIM Investigations of the Adsorption of Chlormethine Anticancer Drug on the Exterior Surface of Pristine and Transition Metal Functionalized Boron Nitride Fullerene, *Journal of Molecular Liquids*, Vol.323, 2021, 114627.

[111] M. Javed Ansari, A. Soltani, M. Ramezanitaghartapeh, P. Singla, M. Aghaei, H. Khandan Fadafan, S. Ardalan Khales, M. Shariati, H. Shirzad-Aski, H. Balakheyli, S. S. Imamh, A. Zafar, Improved Antibacterial Activity of Sulfasalazine Loaded Fullerene Derivative: Computational and Experimental studies, *Journal of Molecular Liquids*, Vol.348, 2022, 118083.

[112] E. E. Ebenso, T. Arslan, F. Kandemirlı, I. Love, C. Ogretır, M. Saracoglu, S. A. Umoren, Theoretical Studies of Some Sulphonamides as corrosion inhibitors for mild steel in acidic medium, *International Journal of Quantum Chemistry*, Vol.110, No.14, 2010, pp. 2614–2636.

[113] U. Özdemir, B. Özbay, S. Veli, S. Zor, Modeling Adsorption of Sodium Dodecyl Benzene Sulfonate (SDBS) onto Polyaniline (PANI) by using Multi Linear Regression and Artificial Neural Networks, *Chemical Engineering Journal*, Vol.178, 2011, pp. 183- 190.

[114] V. V. Nair, H. Dhar, S. Kumar, A. K. Thalla, S. Mukherjee, J. W. C. Wong, Artificial Neural Network-Based Modelling to Evaluate Methane Yield from Biogas in a Laboratory-Scale Anaerobic Bioreactor, *Bioresource Technology*, Vol.217, 2016, pp. 90–99.

[115] W. Uddin, K. Ayeshab, Z. Kamran, H. Aun, K. Bilal, I. Saiful, M. Ishfaqa, K. Imran, M. Adild, K. H. Je, Current and Future Prospects of Small Hydropower in Pakistan: A Survey, *Energy Strategy Reviews*, Vol.24, 2019, pp. 166–177.

[116] C. Rashama, G. Ijoma, T. Matambo, Biogas Generation from By-products of Edible Oil Processing: a Review of Opportunities, Challenges and Strategies, *Biomass Conversion and Biorefinery Journal*, Vol.9, No.4, 2019, pp. 803–826.

[117] K. C. Surendra, D. Takara, A. G. Hashimoto, S. K. Khanal, Biogas as a Sustainable Energy Source for Developing Countries, *Opportunities and Challenges Renewable and Sustainable Energy Reviews*, Vol.31, 2014, pp. 846–859.

[118] R. Arthur, M. F. Baidoo, E. Antwi. Biogas as a Potential Renewable Energy Source: A Ghanaian Case Study, *Renewable Energy*, Vol.13, 2010, pp. 1–7.

[119] M. M. Ghiasi, M. Arabloo, A. H. Mohammadi, T. Barghi, Application of ANFIS Soft Computing Technique in Modelling the CO_2 Capture with MEA, DEA, and TEA Aqueous Solutions, *International Journal of Greenhouse and Gas Control*, Vol.49, 2016, pp. 47–54.

APPENDIX

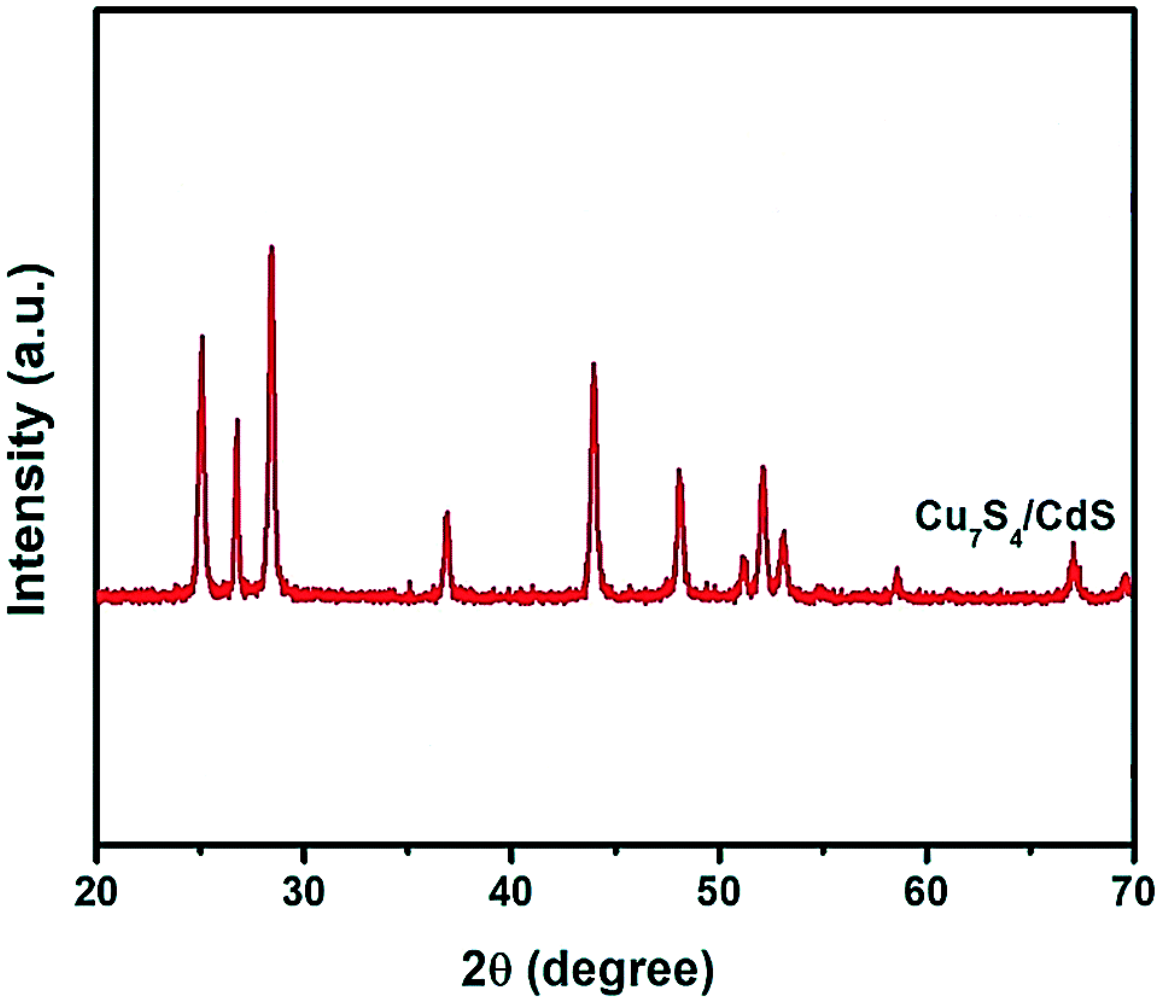

Figure 1. XRD spectra of Cu_7S_4/CdS nanocatalyst after photoreforming process for H_2(g) production from real wastes of PLA.

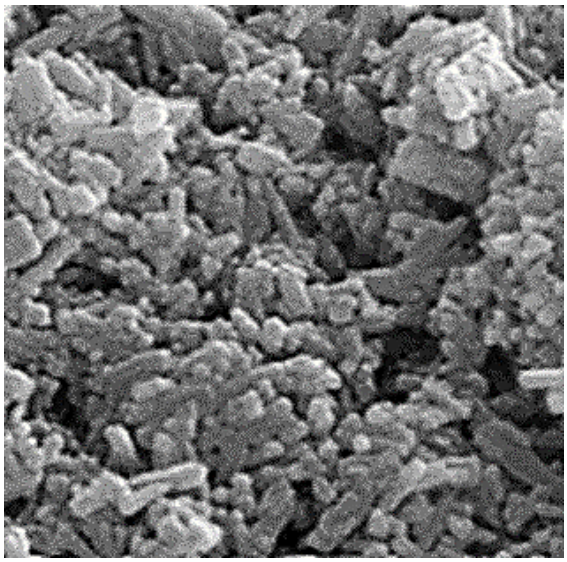

(a)

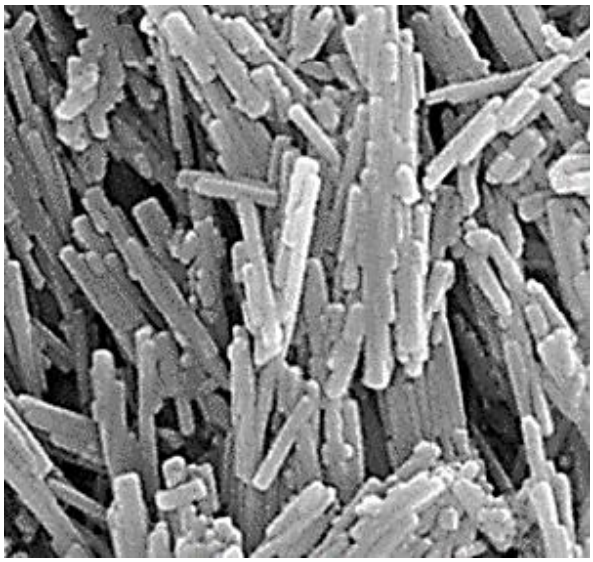

(b)

Figure 2. FESEM images of Cu_7S_4/CdS nanocatalyst **(a)** before photoreforming process (**b)** after photoreforming process for H_2(g) production from real wastes of PLA (FESEM image size: 4 μm).

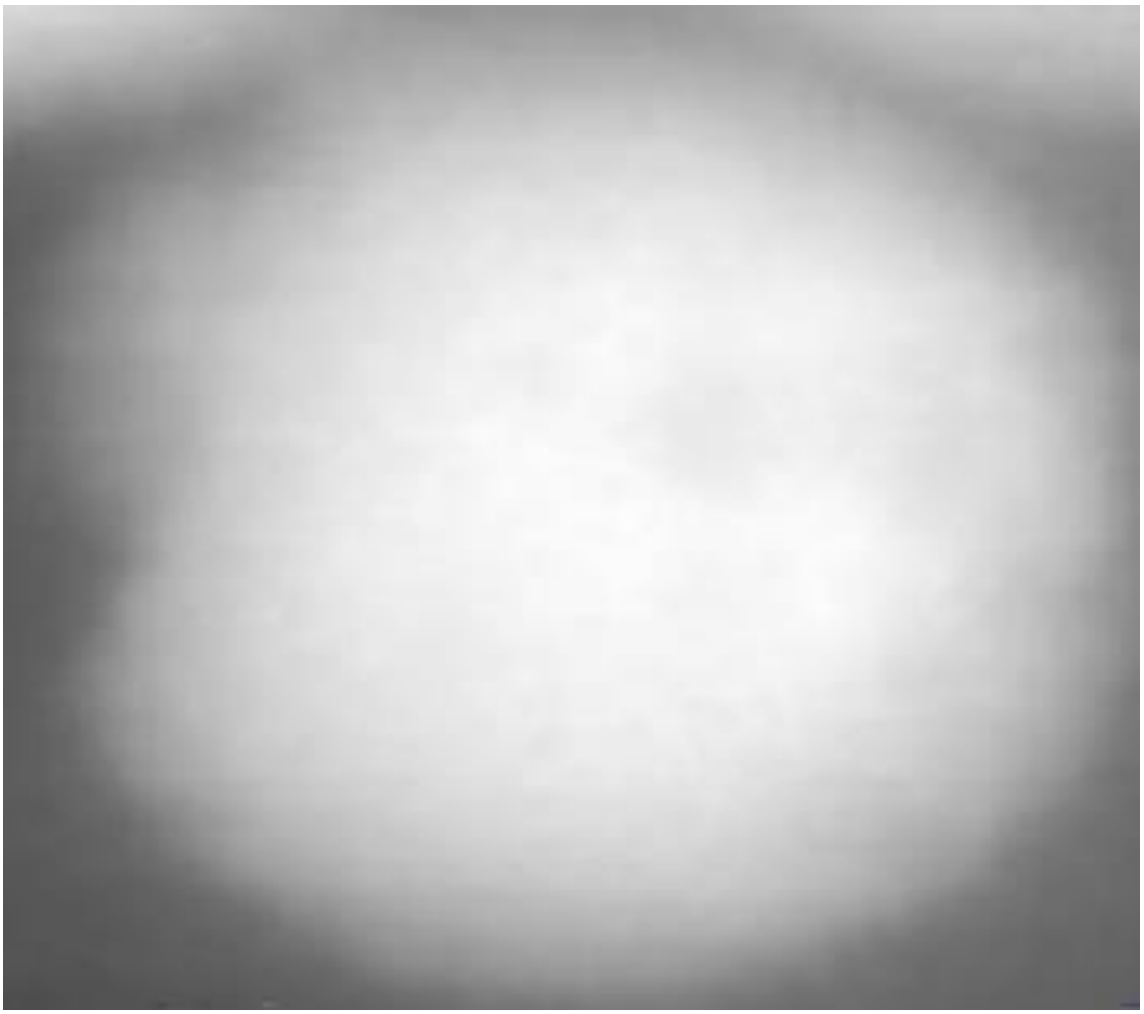

Figure 3. EDX spectrum of Cu_7S_4/CdS nanocatalyst after photoreforming process for H_2(g) production from real wastes of PLA (EDX spectra size: 5 nm).

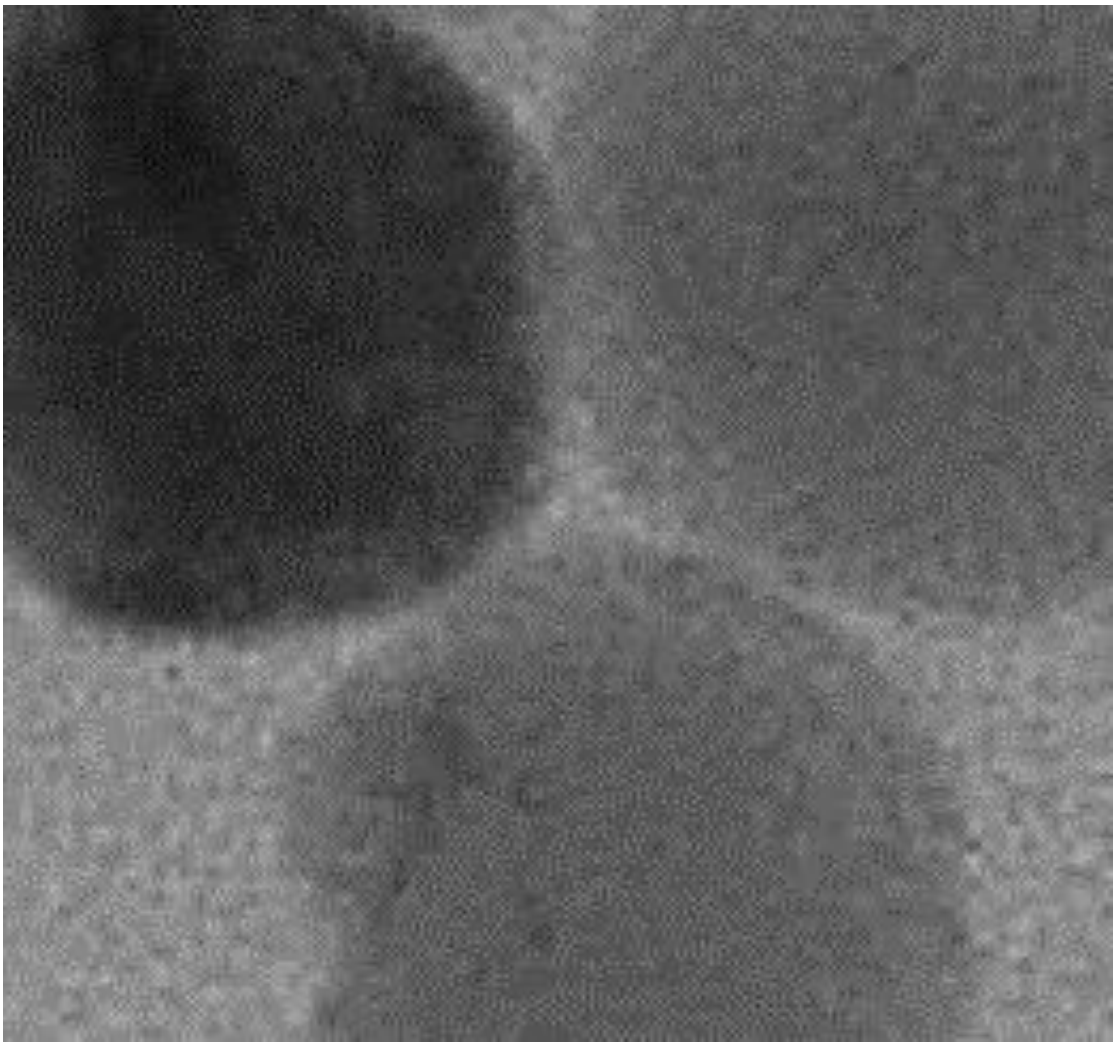

Figure 4. TEM images of Cu_7S_4/CdS nanocatalyst after photoreforming process for H_2(g) production from real wastes of PLA (TEM image size: 5 nm).

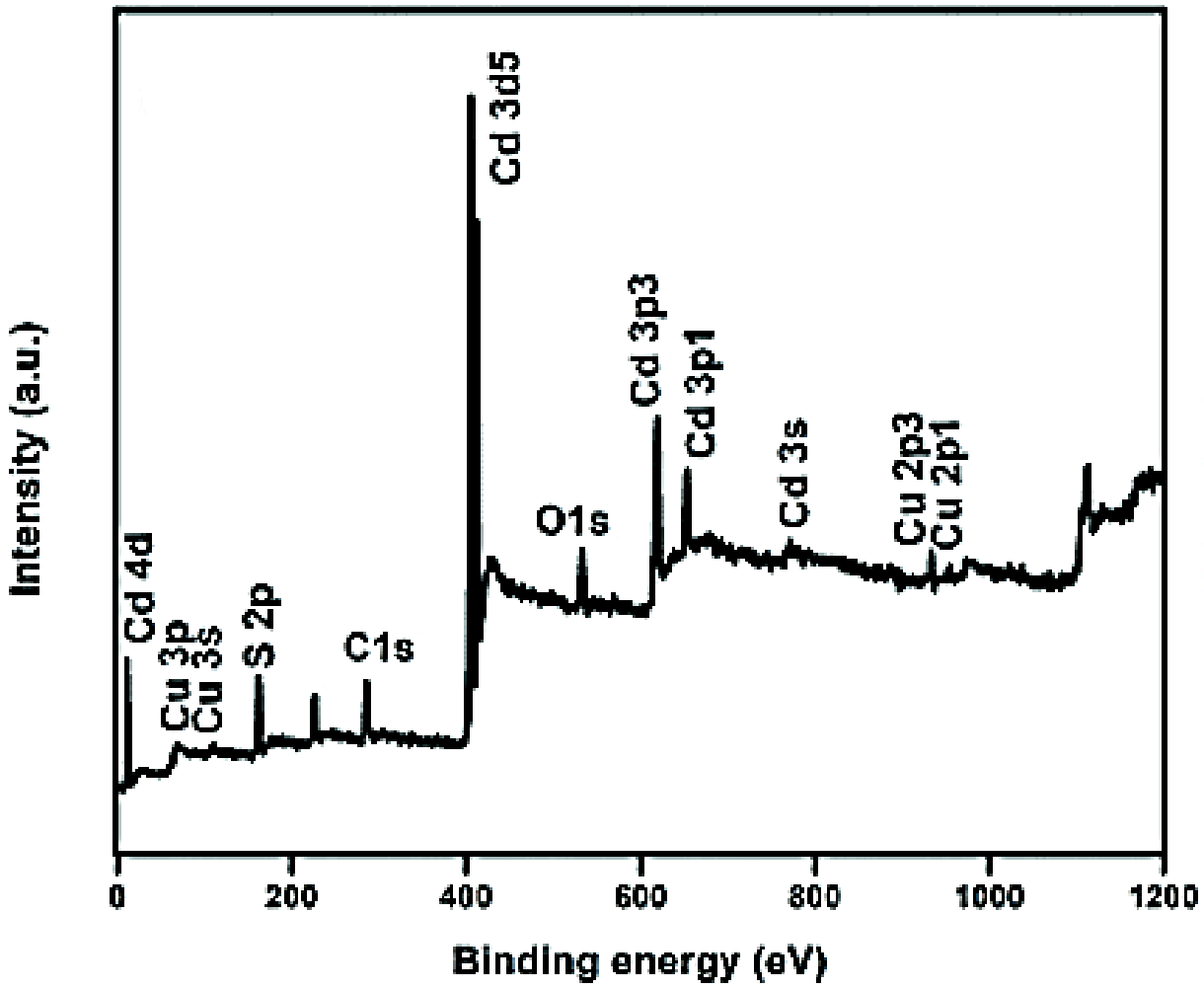

Figure 5. XPS spectra of Cu_7S_4/CdS nanocatalyst after photoreforming process for H_2(g) production from real wastes of PLA.

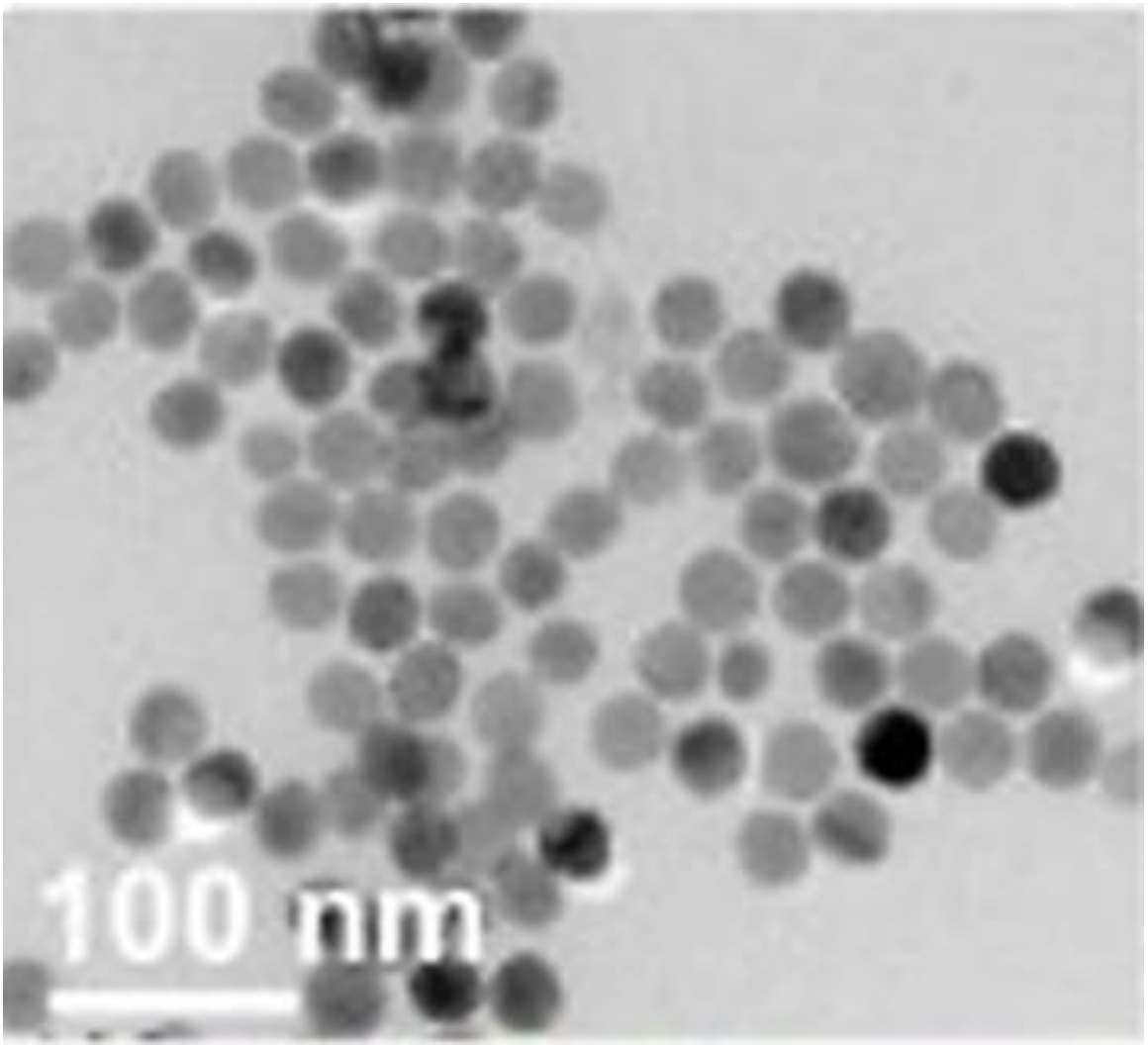

Figure 6. ICP-OES images of Cu_7S_4/CdS nanocatalyst after photoreforming process for H_2(g) production from real wastes of PLA (ICP-OES image size: 100 nm).

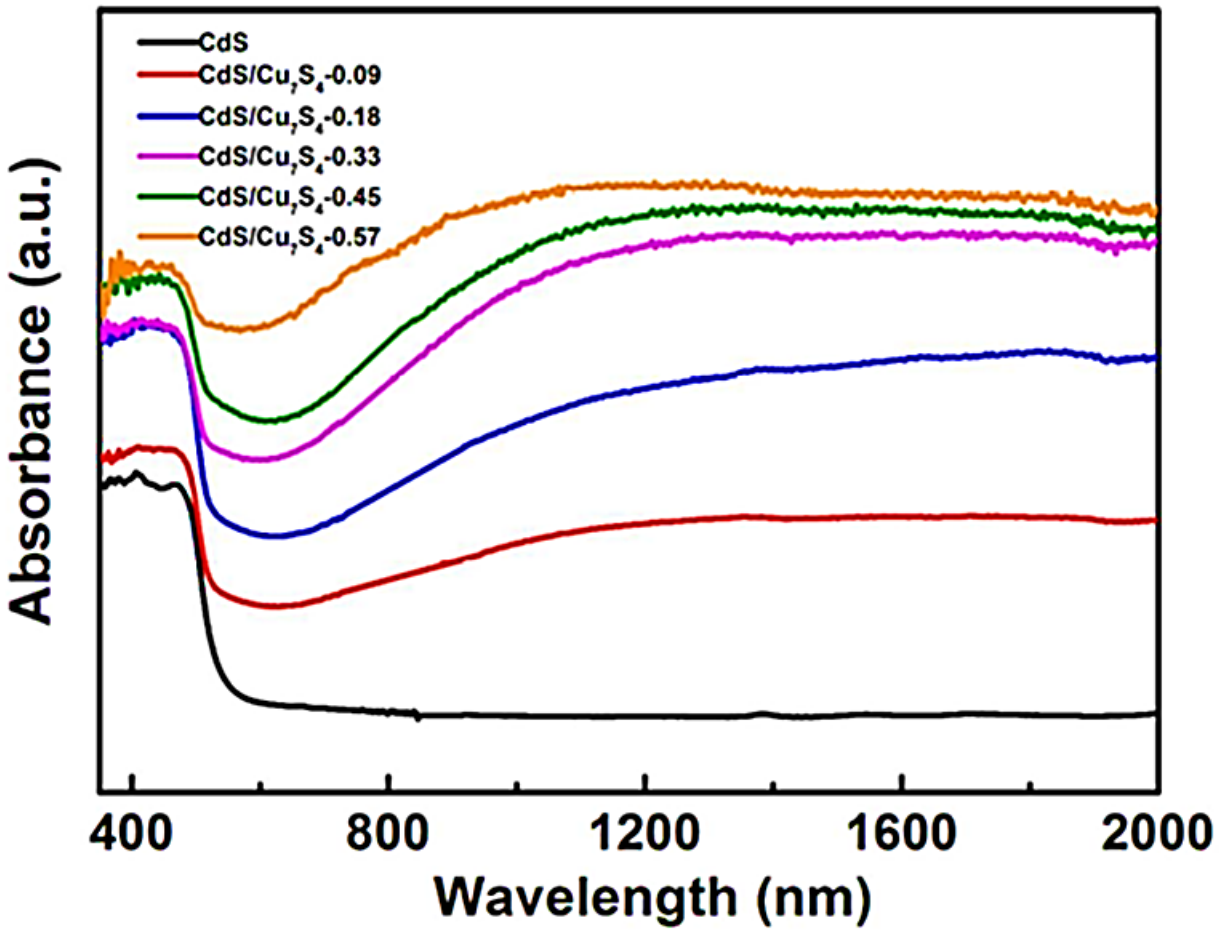

Figure 7. The comparison of UV-vis-NIR DRS spectra of the prepared CdS/Cu_7S_4x (x=0, 0.09, 0.18, 0.33, 0.45, 0.57), respectively.

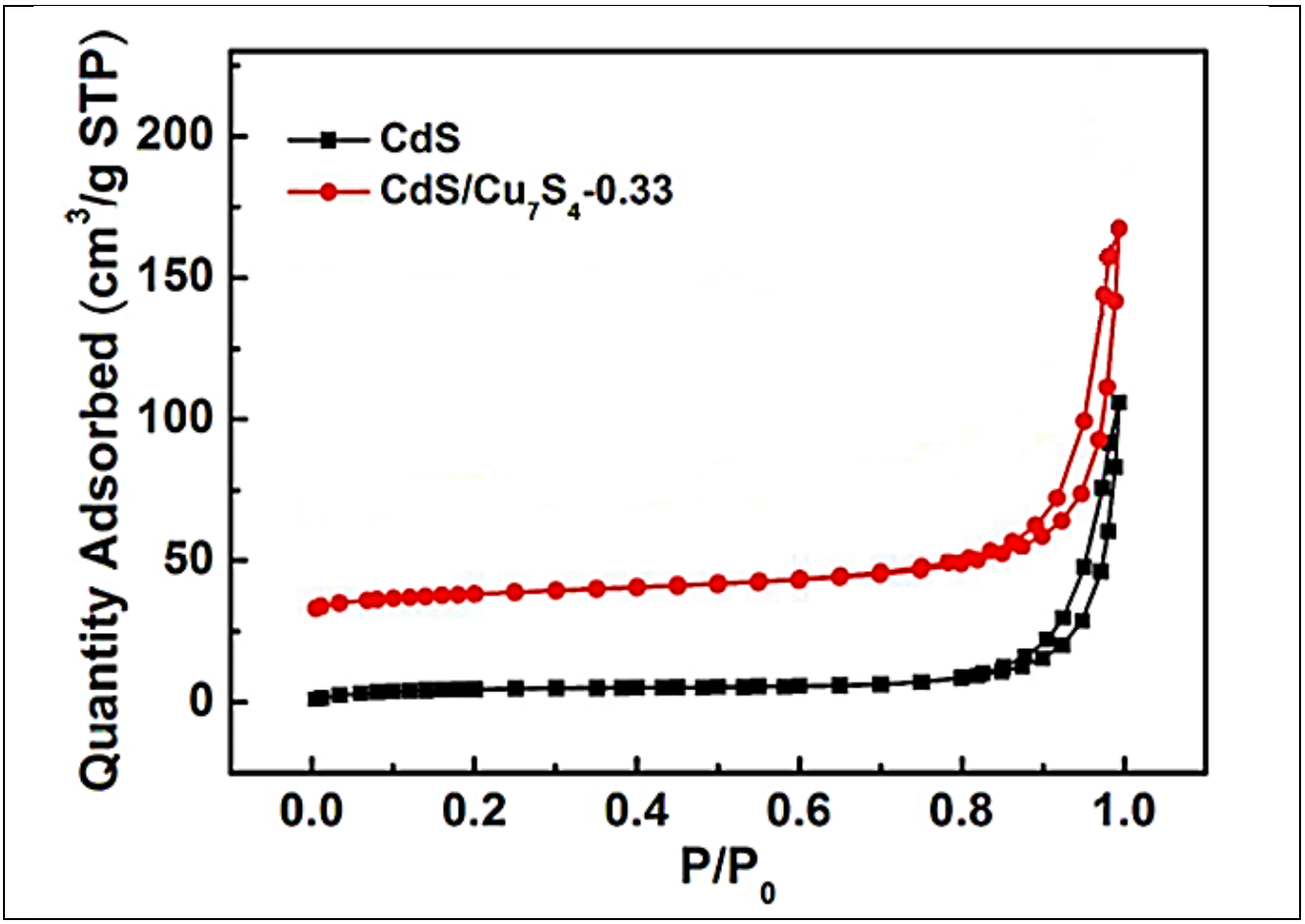

Figure 8. N_2 adsorption-desorption isotherms of CdS and Cu_7S_4/CdS-0.33 heterostructure.

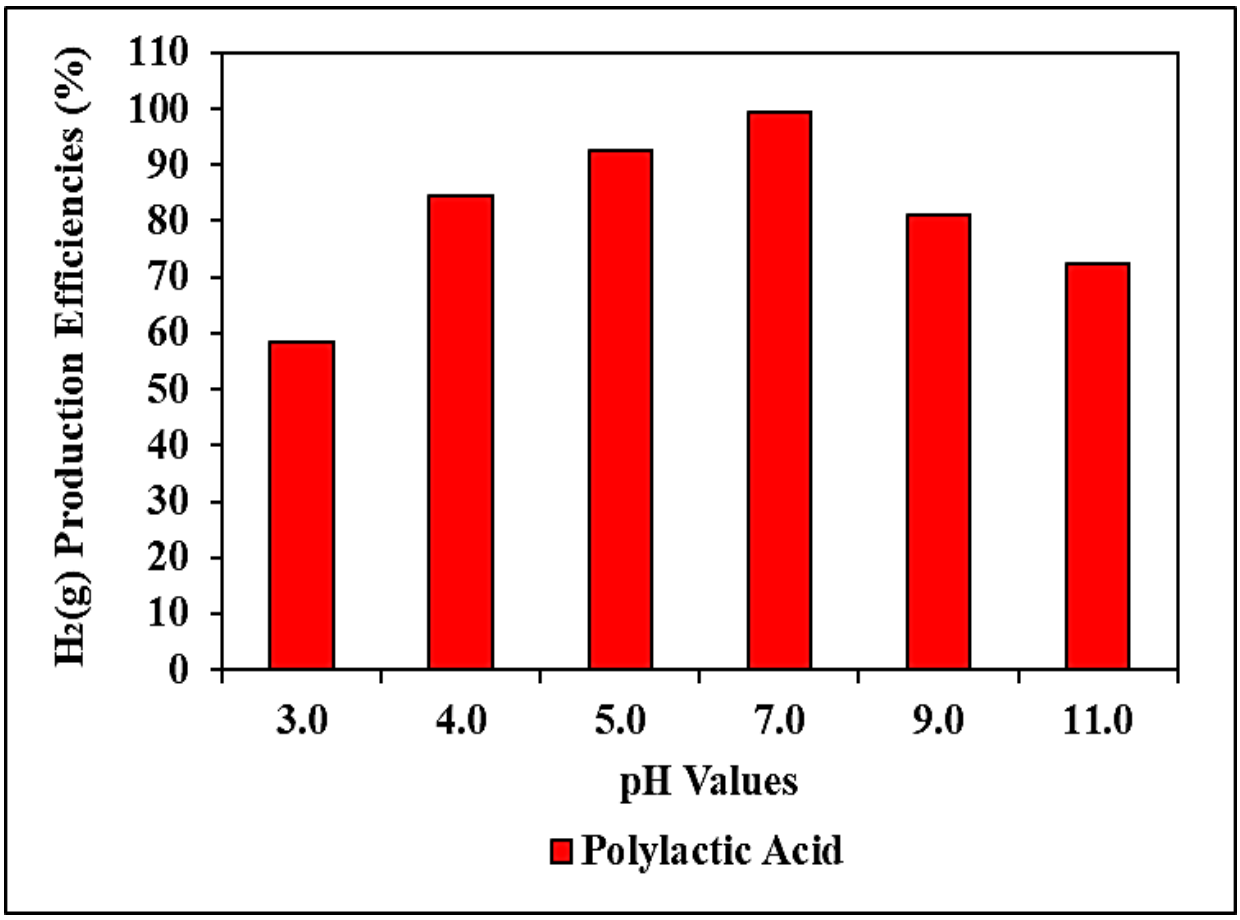

Figure 9. Effect of increasing pH values for $H_2(g)$ production with photocatalytic degradation process from PLA real plastic wastes, at 300 W UV-vis light and at 25°C, respectively (y error bar varied between 1.1% and 1.2%).

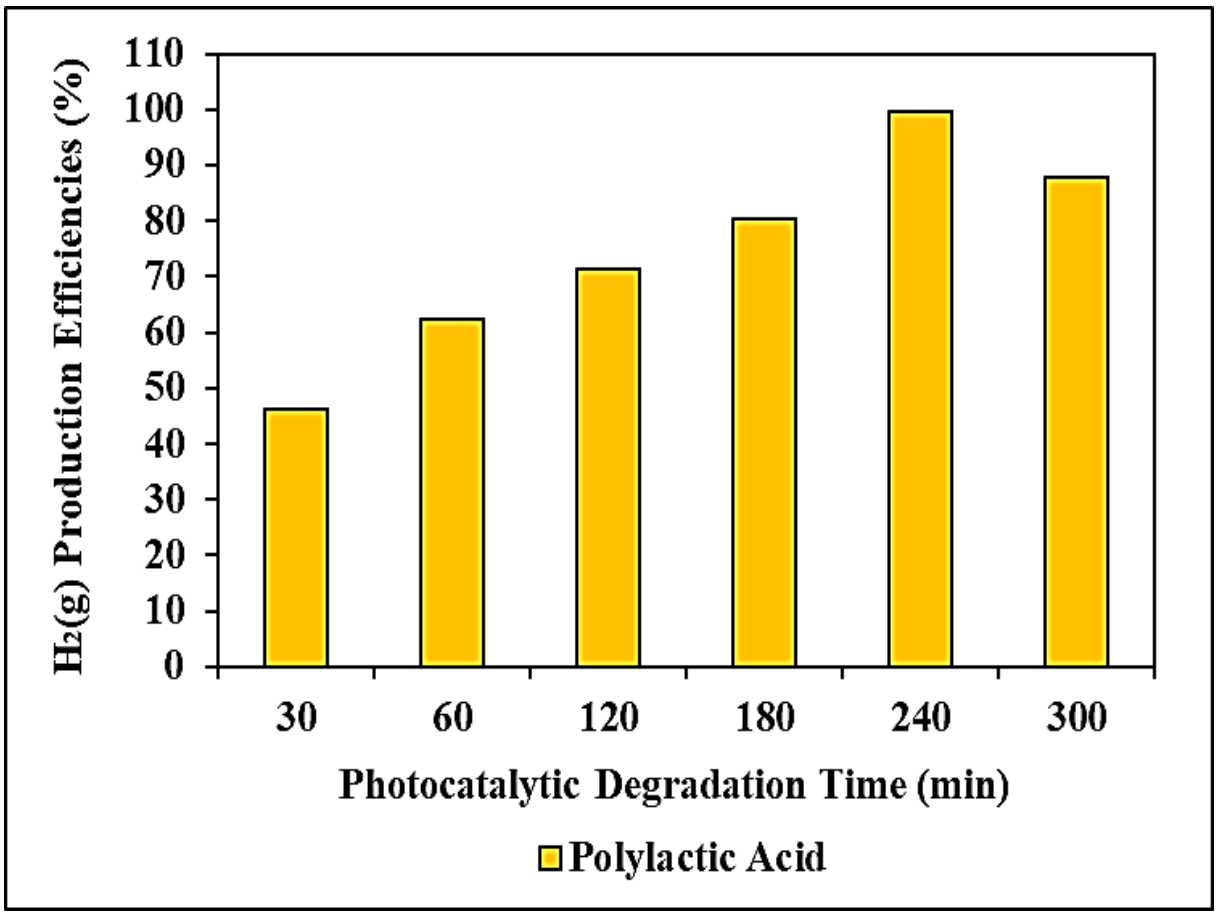

Figure 10. Effect of increasing photocatalytic degradation time for H_2(g) production with photocatalytic degradation process from PLA real plastic wastes, at 300 W UV-vis light, at pH=7.0 and at 25^{o}C, respectively (y error bar varied between 1.1% and 1.3%).

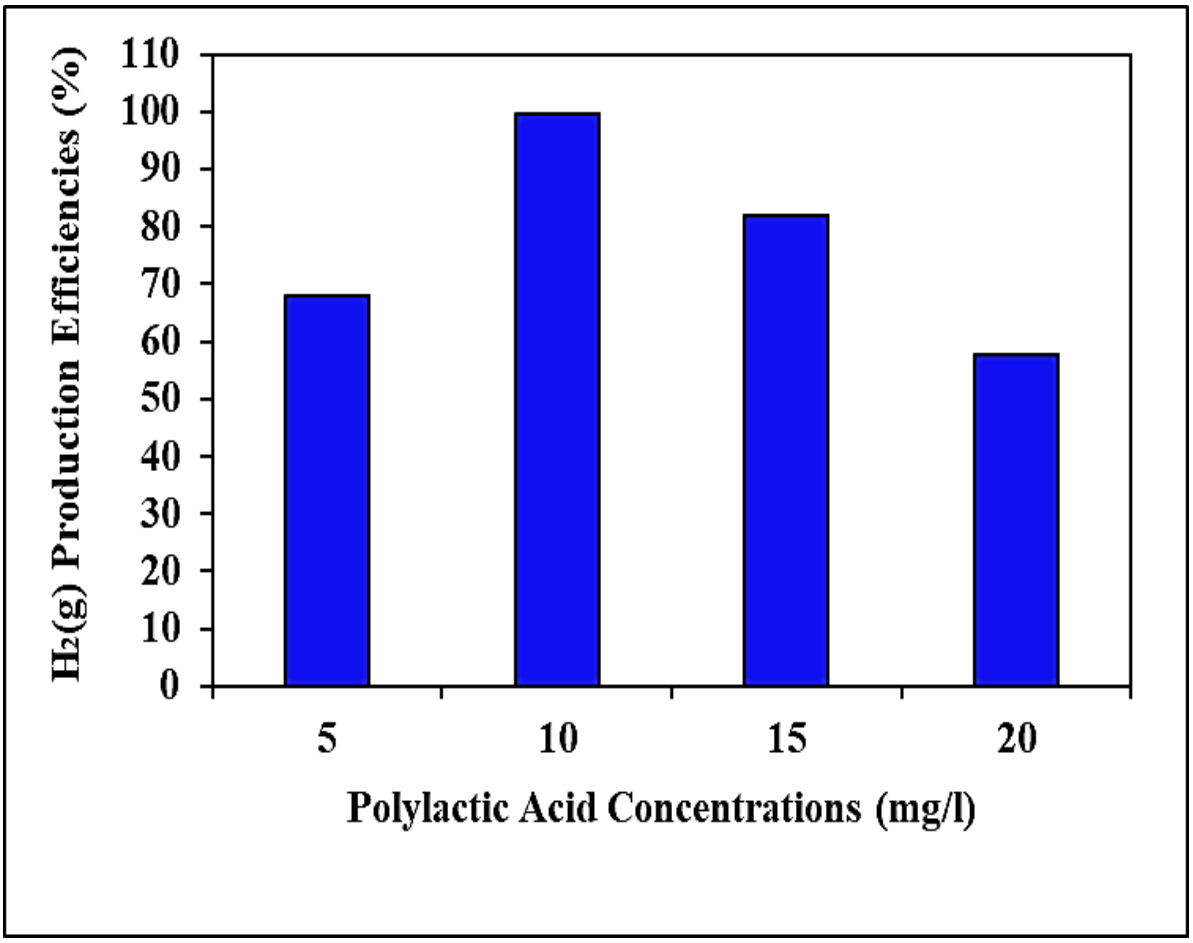

Figure 11. Effect of increasing PLA concentrations for H_2(g) production with photocatalytic degradation process from PLA real plastic wastes, after 240 min, at 300 W UV-vis light, at pH=7.0 and at 25^{o}C, respectively (y error bar varied between 1.1% and 1.2%).

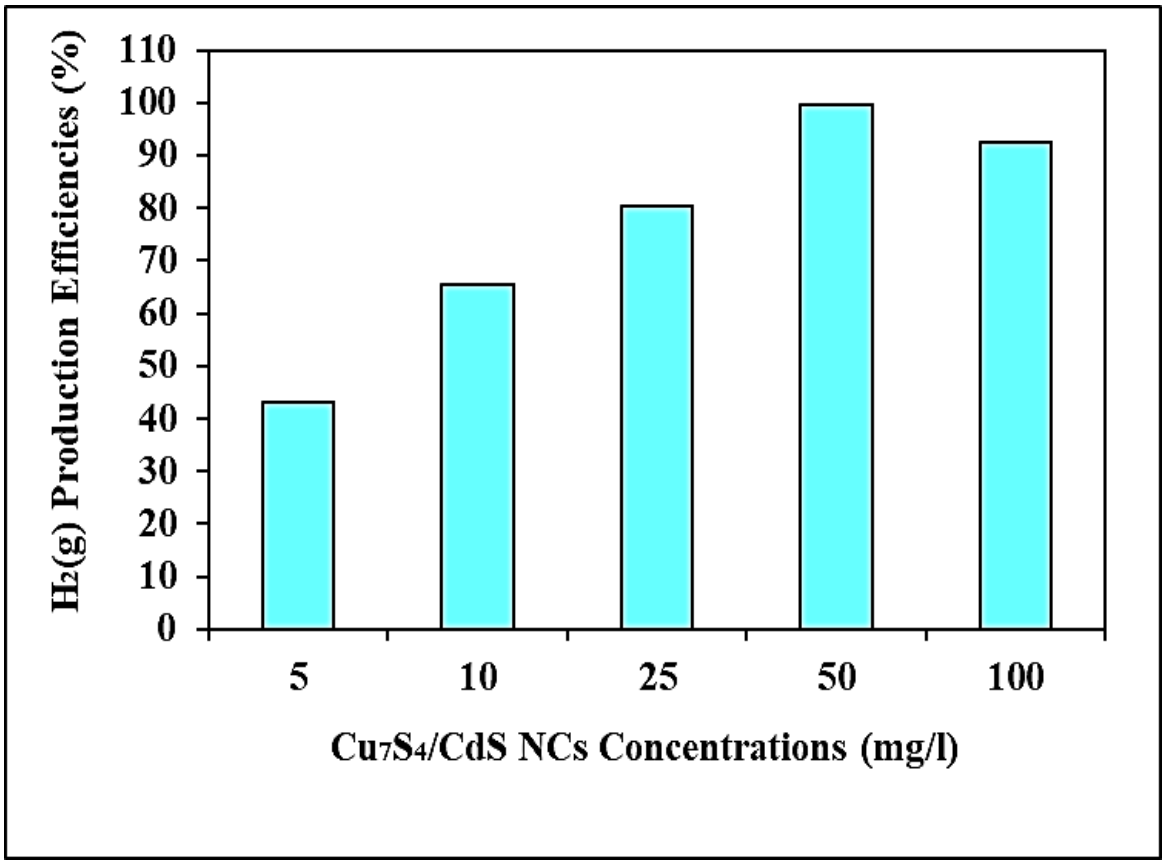

Figure 12. Effect of increasing Cu_7S_4/CdS NCs concentrations for H_2(g) production with photocatalytic degradation process from PLA real plastic wastes, after 240 min, at 10 mg/l PLA, after 240 min, at 300 W UV-vis light, at pH=7.0 and 25ºC, respectively(y error bar varied between 1.0% and 1.2%).

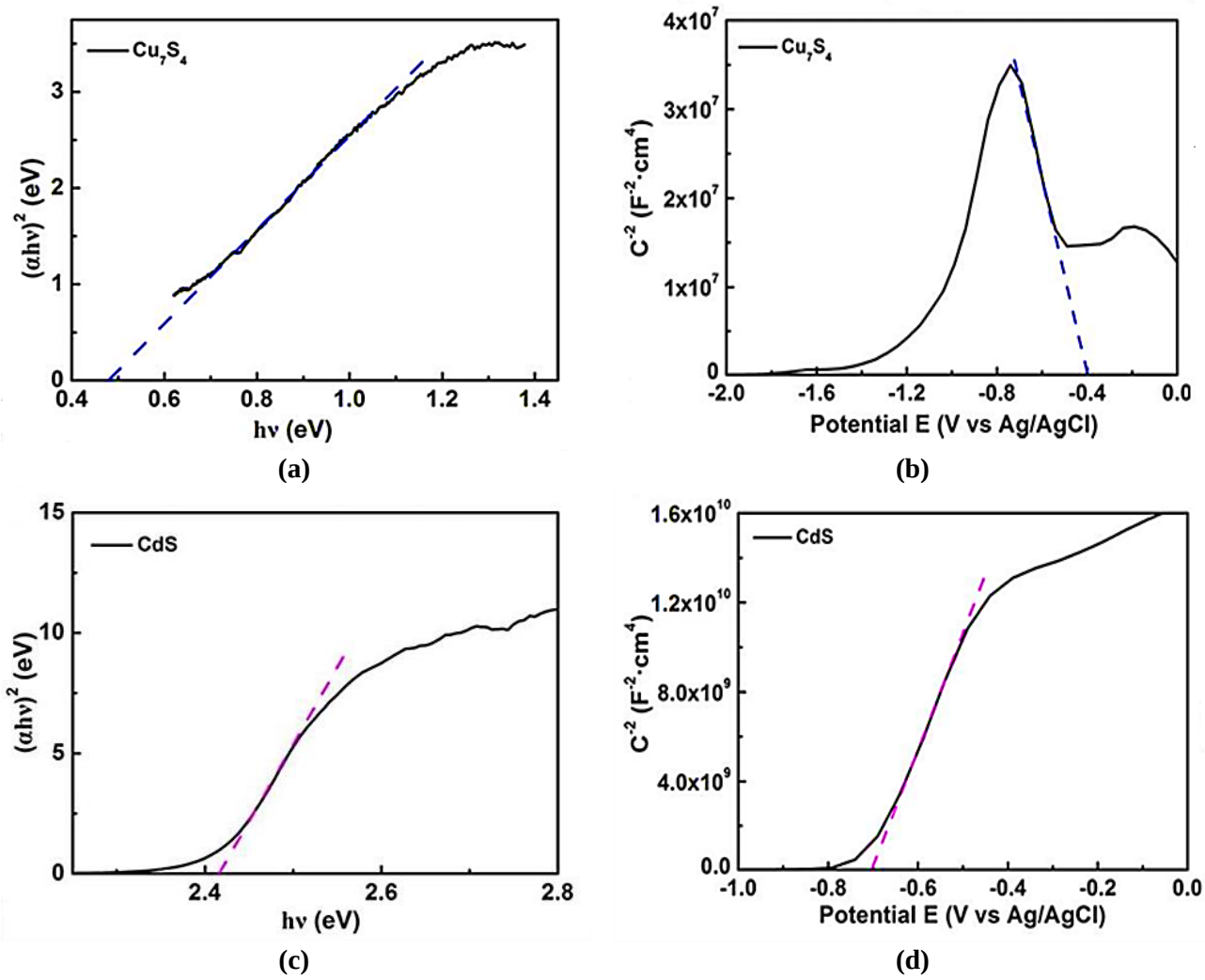

Figure 13. The optical bandgaps and MottSchottky plots for Cu_7S_4 (**a** and **b**), CdS (**c** and **d**), respectively.

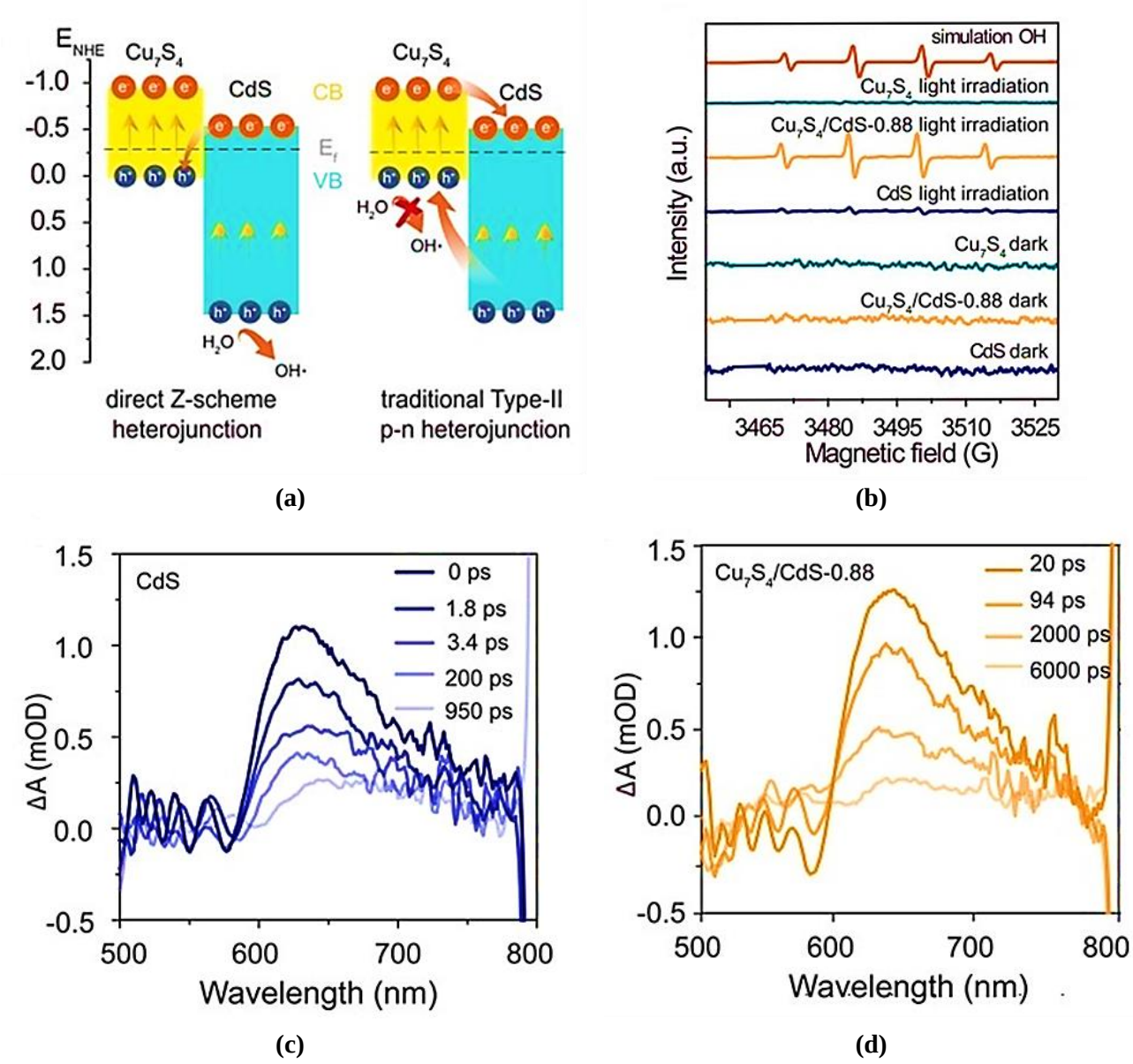

Figure 14. (a) Illustration for direct Z-scheme heterojunction and traditional type-II heterojunction electron transfer mechanism; **(b)** EPR spectra of $OH^{\bullet}$·radicals formed during the photocatalytic H_2 evolution; **(c)** and **(d)** TA spectra of CdS and Cu_7S_4/CdS-0.88 after excitation at 400 nm, respectively.

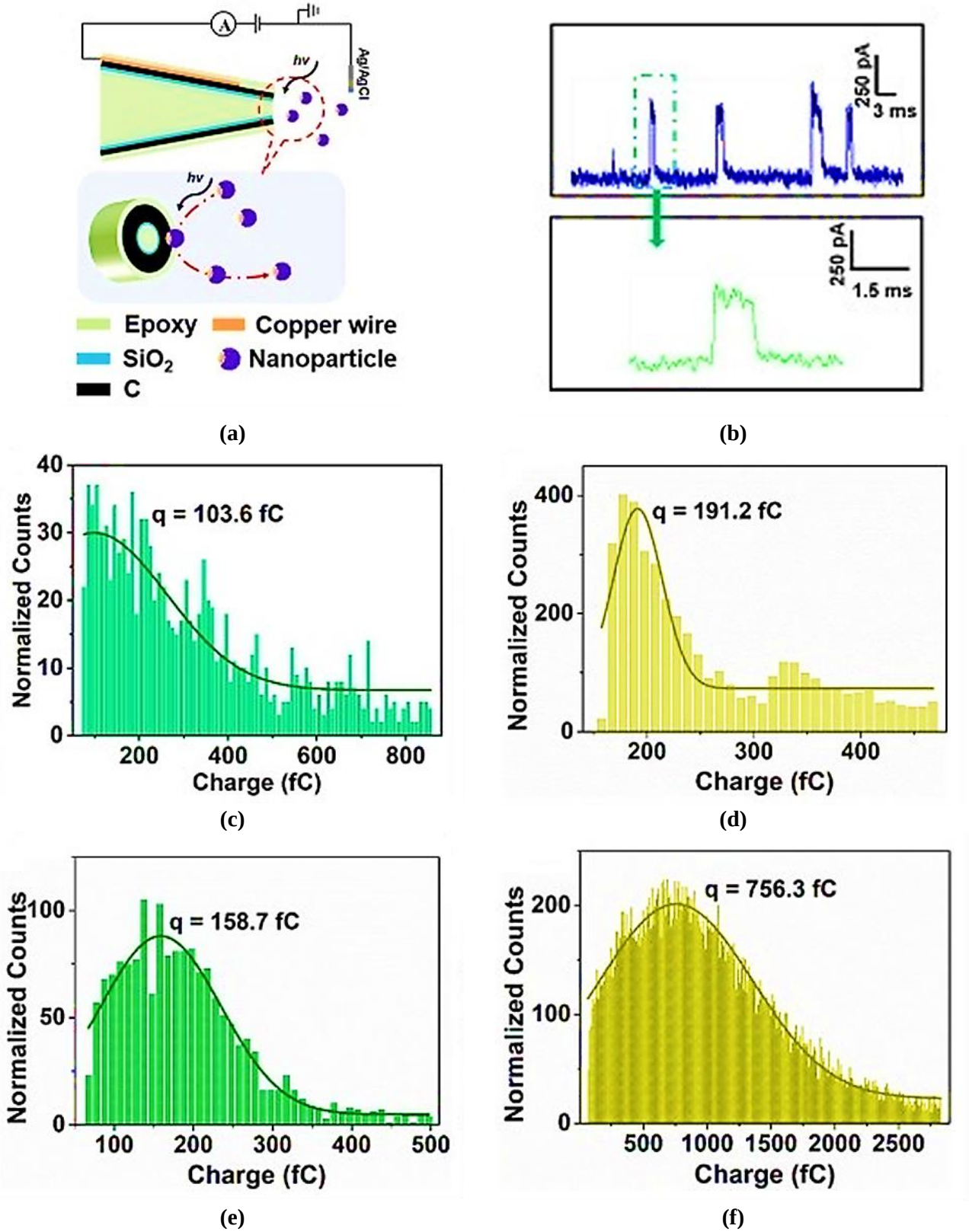

Figure 15. Illustration of electrochemistry experimental set up for **(a)** monitoring collisions of a NP with a microelectrode; **(b)** example section of original current transients for analyses and a zoom-in 20 ms long portion of the same recording; **(c)** and **(d)** Current transient distribution produced by collisions of multiple Cu_7S_4/CdS-0.46 and Cu_7S_4/CdS-0.88 NCs with the microelectrode under dark; **(e)** and **(f)** Current transient distribution produced by collisions of multiple Cu_7S_4/CdS-0.46 and Cu/Cd-0.88 NCs with the microelectrode under visible light (> 420 nm) irradiation.

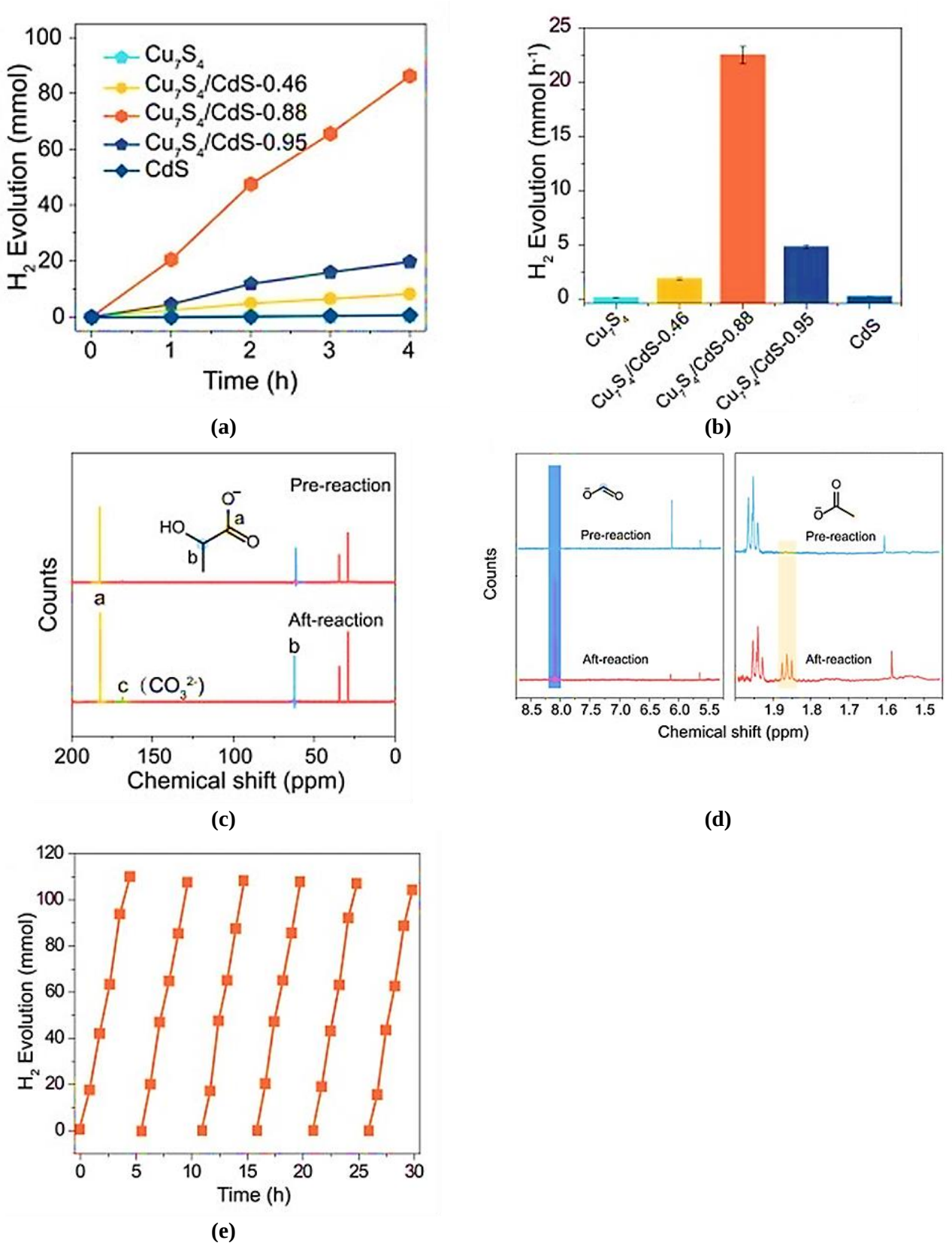

Figure 16. (a) Photocatalytic H_2 evolution activities of Cu_7S_4/CdS heterojunction catalysts with different Cd content under visible-light irradiation (> 420nm) waste plastic as feedstock; **(b)** Comparison of photocatalytic H_2 generation activities of Cu_7S_4/CdS heterojunction catalysts with different Cd content during 4 h; **(c)** and **(d)** ^{1}H-NMR and ^{13}C-NMR spectra of PLA before (pre-PR) and after (Aft-PR) 4 h irradiation; **(e)** Recycled H_2 evolution property of Cu_7S_4/CdS-0.88, respectively.

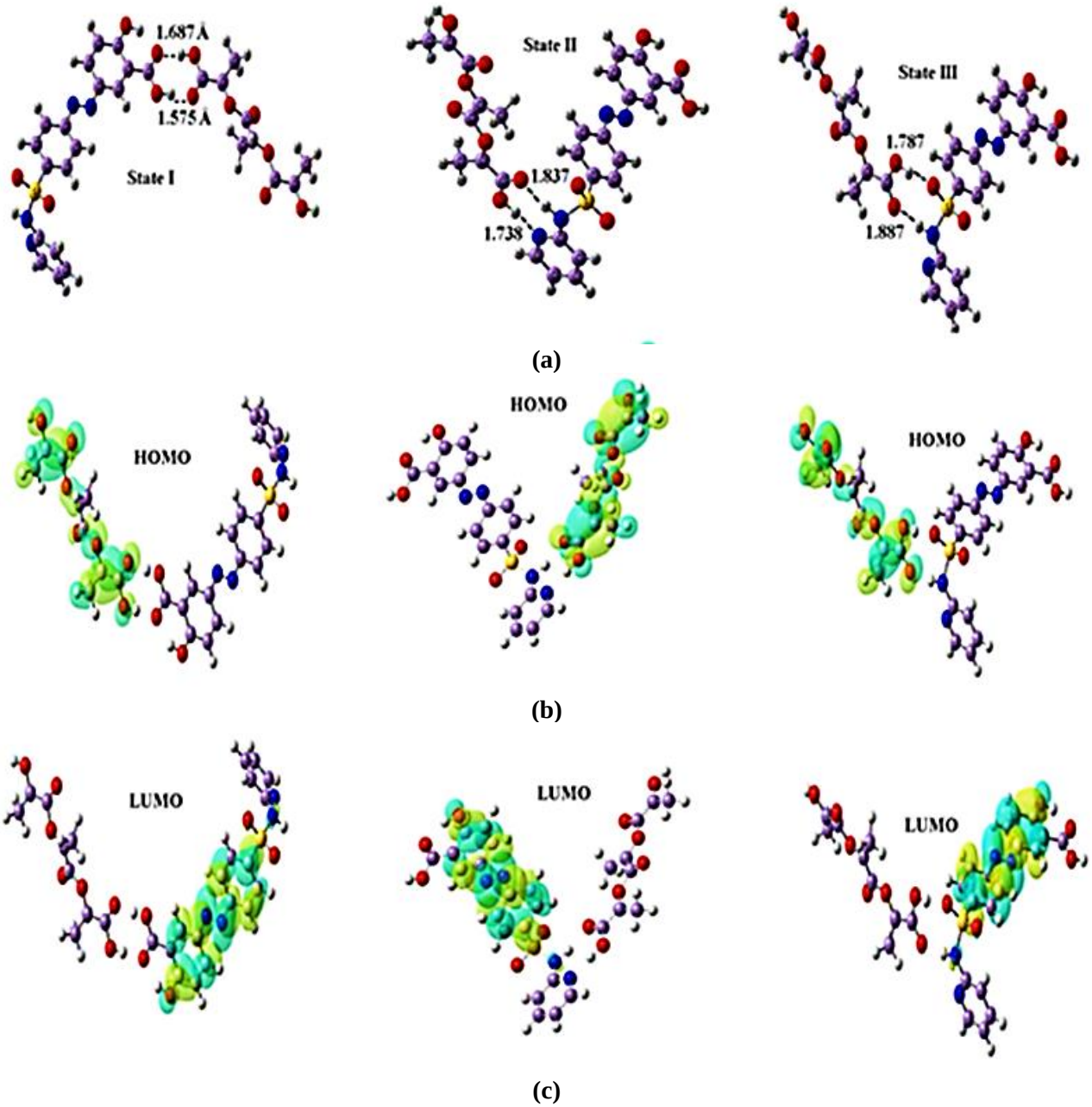

Figure 17. Optimized geometric structures **(a)**, HOMO **(b)**, and LUMO **(c)** plots of C_7S_4/CdS NCs molecule with PLA carrier in State I, II, and III complexes.

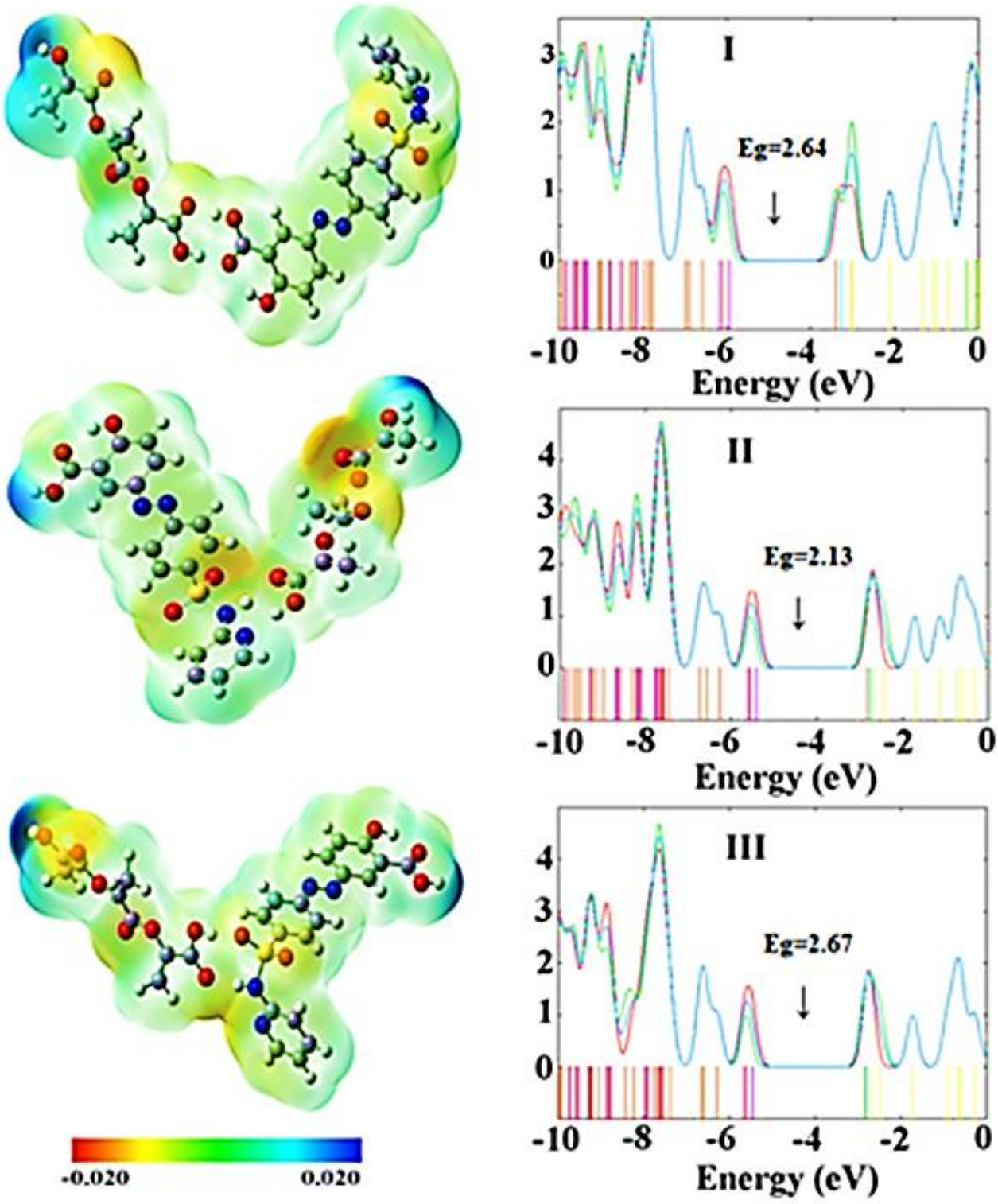

Figure 18. The molecular electrostatic potential **(a)** and density of states **(b)** of C_7S_4/CdS NCs interacting with PLA carrier in the three states.

Table 1. Calculated binding energy (E_{bin}), dipole moment (DM), HOMO energy (E_{HOMO}), LUMO energy (E_{LUMO}), energy gap (E_g), change of energy gap (ΔE_g) and Fermi level energy (E_F) for Cu_7S_4/CdS NCs and PLA, their complexes.

Property	**E_{bin} (eV)**	**DM (Debye)**	**E_{HOMO} (eV)**	**E_{LUMO} (eV)**	**E_g (eV)**	**ΔE_g (%)**	**E_F (eV)**
Cu_7S_4/CdS NCs	-	7.30	- 6.31	- 2.70	3.61	-	- 4.51
PLA	-	5.12	- 5.45	- 2.77	2.65	-	- 4.13
Stage I	- 0.71	13.98	- 5.93	- 3.29	2.64	0.38	- 4.61
Stage II	- 0.64	8.34	- 5.42	- 2.74	2.13	19.62	- 4.36
Stage III	- 0.51	7.77	- 5.47	- 2.80	2.67	0.75	- 4.14

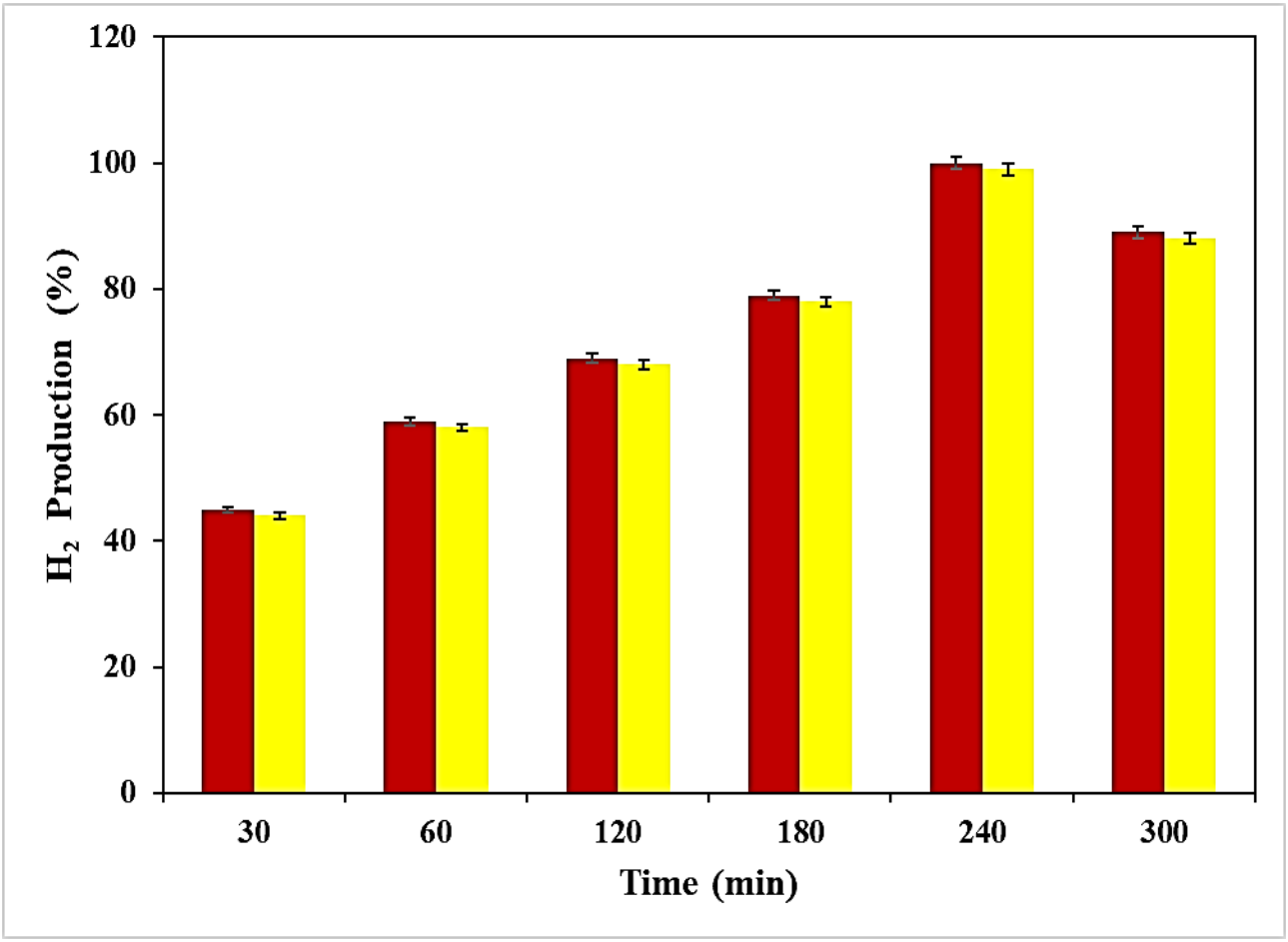

Figure 19. Comparison of experimental and ANN model data during photocatalytic time with y error bars.

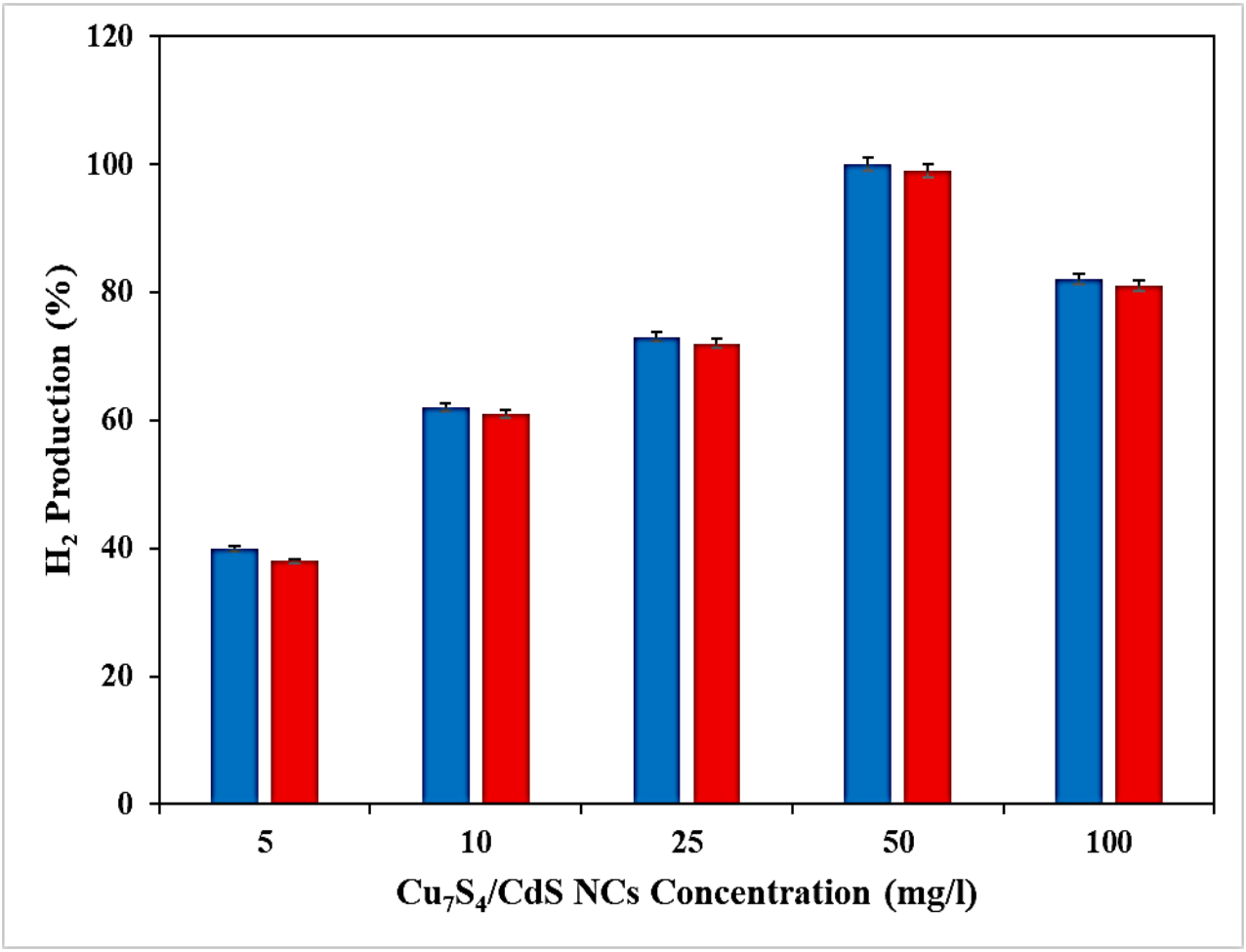

Figure 20. Comparison of experimental and ANN model data during increasing nanocomposite concentration with y error bars.

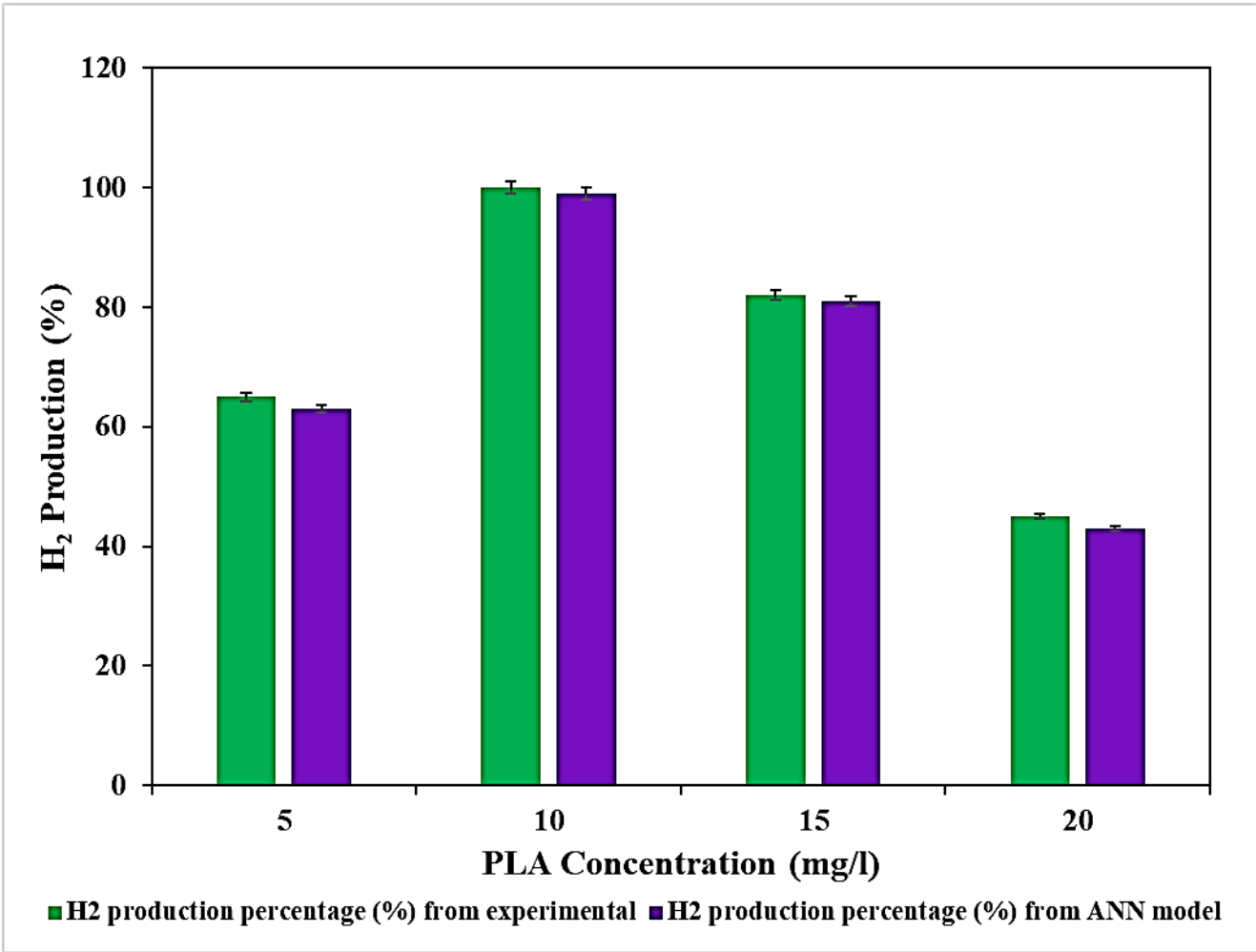

Figure 21. Comparison of experimental and ANN model data during increasing PLA concentration with y error bars.

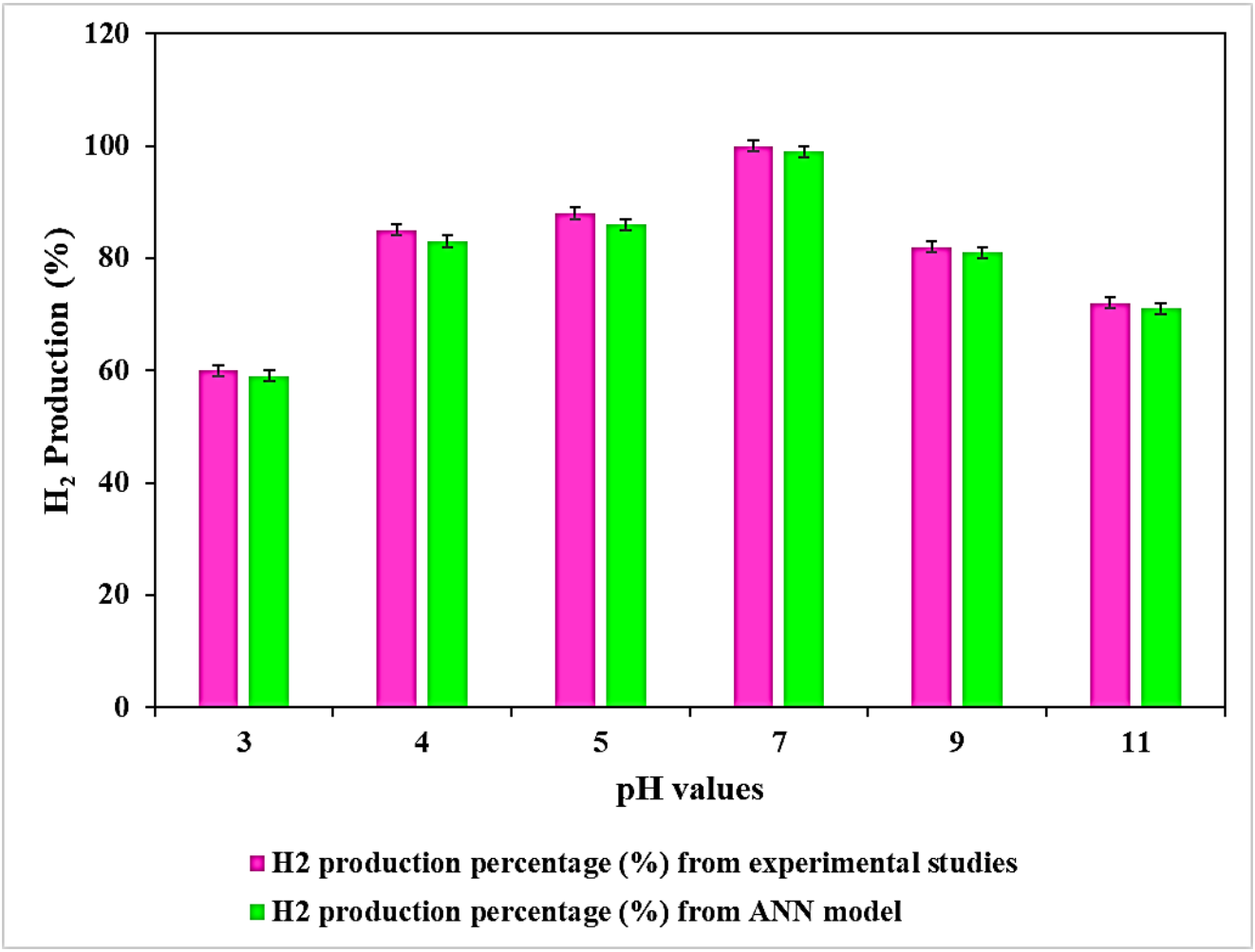

Figure 22. Comparison of experimental and ANN model data during increasing pH values with y error bars.

Table 2. Reusability of 50 mg/l Cu_7S_4/CdS NCs during 10 mg/l PLA degradation.

Cycles	**Reusability efficiency (%)**
1	99
2	99
3	99
4	99
….	99
….	99
….	99
…	99
28	99
29	99
30	99
31	99
32	99
33	99
34	99
35	98
36	98
37	98
38	98
39	98
40	98